

Understanding and Enhancing Encoder-based Adversarial Transferability against Large Vision-Language Models

Xinwei Zhang*

The Hong Kong Polytechnic University
Hong Kong, China
xin-wei.zhang@connect.polyu.hk

Youqian Zhang

The Hong Kong Polytechnic University
Hong Kong, China
you-qian.zhang@polyu.edu.hk

Ruochen Du

Harbin Engineering University
Harbin, China
drc96@hrbeu.edu.cn

Li Bai

The Hong Kong Polytechnic University
Hong Kong, China
baili.bai@connect.polyu.hk

Qingqing Ye

The Hong Kong Polytechnic University
Hong Kong, China
qingqing.ye@polyu.edu.hk

Haibo Hu†

The Hong Kong Polytechnic University
Hong Kong, China
haibo.hu@polyu.edu.hk

Tianwei Zhang

Nanyang Technological University
Singapore
tianwei.zhang@ntu.edu.sg

Yingnan Zhao

Harbin Engineering University
Harbin, China
zhaoyingnan@hrbeu.edu.cn

Abstract

Large vision-language models (LVLMs) have achieved impressive success across multimodal tasks, but their reliance on visual inputs exposes them to significant adversarial threats. Existing encoder-based attacks perturb the input image by optimizing solely on the vision encoder, rather than the entire LVLM, offering a computationally efficient alternative to end-to-end optimization. However, their transferability across different LVLM architectures in realistic black-box scenarios remains poorly understood. To address this gap, we present the *first* systematic study towards encoder-based adversarial transferability in LVLMs. Our contributions are threefold. First, through large-scale benchmarking over eight diverse LVLMs, we reveal that existing attacks exhibit severely limited transferability. Second, we perform in-depth analysis, disclosing two root causes that hinder the transferability: (1) *inconsistent visual grounding across models*, where different models focus their attention on distinct regions; (2) *redundant semantic alignment within models*, where a single object is dispersed across multiple overlapping token representations. Third, we propose Semantic-Guided Multimodal Attack (SGMA), a novel framework to enhance the transferability. Inspired by the discovered causes in our analysis, SGMA directs perturbations toward semantically critical regions and disrupts cross-modal grounding at both global and local levels. Extensive experiments across different victim models and tasks show that SGMA achieves higher transferability than existing attacks. These results expose critical security risks in LVLM deployment and underscore the urgent need for robust multimodal defenses.

CCS Concepts

- Security and privacy → Software and application security;
- Computing methodologies → Neural networks.

Keywords

Large vision-language models; encoder-based transferability; adversarial examples

1 Introduction

With the rapid advancement of data scale, computational resources, and model architectures, large language models (LLMs) have demonstrated impressive capabilities in understanding and generating natural language. Building upon the semantic reasoning capabilities of LLMs, large vision-language models (LVLMs), such as GPT-4V [41] and Gemini [20], incorporate visual inputs to support multiple modalities, thereby significantly enhancing instruction following and user interaction in complex vision-language scenarios. However, the visual modality is inherently more susceptible to imperceptible perturbations compared to the textual modality [12, 22, 42, 77], which could amplify the vulnerability of the LVLM to adversarial examples. This raises serious security concerns for deploying LVLMs in safety-critical applications, such as medical image analysis [31, 38] and autonomous systems [35].

Researchers have proposed a variety of attacks against LVLMs by generating adversarial vision input. A straightforward attack strategy is end-to-end optimization [48], where perturbations are directly crafted based on the model’s final output. This approach is typically model-specific and computationally expensive since it requires access to the full forward and backward pass of the entire LVLM [10]. As a more lightweight alternative, recent efforts have shifted toward encoder-based attacks, which perturb the input image by targeting only the vision encoder of the LVLM

*Part of this work is conducted during a visit to Nanyang Technological University.

†Corresponding author.

[10, 13, 53, 56]. These methods leverage the property of *encoder-based transferability*, i.e., adversarial perturbations effective on a surrogate vision encoder are expected to remain effective in different victim LVLMs. In most studies, this property relies on the strong assumption [10, 55, 56, 66] that the victim LVLM shares the same or a highly similar vision encoder with the surrogate. However, the effectiveness of adversarial attacks against LVLMs with heterogeneous architectures in encoders and language modules, which reflects a more realistic scenario [9, 25, 40], is less explored.

In this work, we present a systematic study of encoder-based adversarial transferability in LVLMs. In particular, we make the following three contributions. First, we benchmark the transferability of existing untargeted encoder-based attacks across eight LVLMs, spanning six open-source models and two commercial services (**Section 3**). Our results reveal that current encoder-based attacks exhibit limited transferability, especially when the victim model adopts a different vision encoder and integrates an advanced language module.

Second, we conduct an in-depth analysis of the observed limited transferability (**Section 4**). This analysis reveals two root causes that lead to the ineffectiveness of existing attacks. ① *Inconsistent visual grounding across models*. Surrogate vision encoders and victim LVLMs focus on distinct image regions, making the perturbations crafted from the surrogate ineffective when transferred to the victim model. ② *Redundant semantic alignment within models*. A single object is typically represented by multiple overlapping tokens, meaning that effective attacks must perturb all of them rather than just a subset. Our failure analysis on the representative encoder-based attack further confirms these causes in practice: perturbations frequently drift toward inconsistent background regions (reflecting root cause ①) or appear too sparse within semantic areas (reflecting root cause ②), both of which prevent them from propagating effectively through the LVLM pipeline. These findings highlight the intrinsic limitations of existing encoder-based attacks, motivating the need for a new attack framework that can overcome both inconsistent grounding and redundant alignment.

Third, motivated by these insights, we propose **Semantic-Guided Multimodal Attack (SGMA)**, a framework specifically designed to enhance adversarial transferability across LVLMs (**Section 5**). SGMA comprises two core components, tackling the two root causes respectively. Specifically, ① *Semantic Relevance Perturbation* anchors the perturbations to patches aligned with the image’s textual description, ensuring they concentrate on foreground regions that are consistently attended across models. ② *Semantic Grounding Disruption* applies global- and local-level perturbations to break redundant cross-modal alignment. By pushing the adversarial image embedding away from its clean counterpart globally and perturbing regions aligned with noun phrases locally, this component ensures that overlapping tokens are comprehensively disrupted, making the perturbations dense enough to break redundant alignment.

We evaluate SGMA over multiple vision–language tasks, including image captioning, visual question answering, and image classification. SGMA consistently outperforms existing attacks across a diverse suite of open-source and commercial LVLMs, achieving higher transferability without compromising perceptual quality. Beyond untargeted attacks, SGMA also extends naturally to the targeted setting, underscoring its flexibility and broad applicability.

In summary, our contributions are: ① We present the first systematic study of encoder-based adversarial transferability across LVLMs in a zero-query black-box setting. ② We perform a comprehensive benchmarking of existing encoder-based adversarial attacks across eight diverse LVLMs, revealing their severely limited transferability. ③ We disclose two root causes that limit encoder-based adversarial transferability in LVLMs: *inconsistent visual grounding across models* and *redundant semantic alignment within models*, which offer new insights into the failure modes of existing attacks. ④ We introduce SGMA, a semantic-guided multimodal attack framework that reallocates perturbations toward semantically critical regions and disrupts cross-modal grounding at both global and local levels. ⑤ Our experiments show that SGMA improves both attack success rate and transferability across multiple LVLMs and tasks.

2 Preliminary

2.1 Large Vision-Language Models

A typical LVLM F_θ consists of three components: a vision encoder f_ϕ that extracts patch-level visual features, a modality projector M_ψ that maps visual embeddings into the textual embedding space, and a large language model L_τ that performs reasoning and text generation. Formally, given an image I and a text prompt T , the LVLM output y is computed as

$$y = F_\theta(I, T) = L_\tau(M_\psi(f_\phi(I)), T). \quad (1)$$

Different LVLMs mainly differ in the design of these three components, and this architectural heterogeneity also complicates adversarial transferability across LVLMs.

2.2 Adversarial Examples against LVLMs

Adversarial examples add imperceptible perturbations to inputs to induce incorrect model behaviors [11, 27]. For LVLMs, perturbations on the image can propagate through the vision–language pipeline and alter the generated text [10, 56]. Since images are easier to manipulate in practice and are highly susceptible to subtle perturbations, most LVLM attacks perturb the image while keeping the prompt unchanged [10, 13, 53, 56, 77]. Formally, given a clean image I and a fixed prompt T , the goal is to find δ such that

$$F_\theta(I + \delta, T) \neq y, \quad \text{s.t. } \|\delta\|_p \leq \epsilon. \quad (2)$$

Existing attacks mainly differ in which part of the model they optimize against. **End-to-end attacks** optimize δ to directly change the final LVLM outputs [13, 48]: $\max_{\|\delta\|_p \leq \epsilon} \mathcal{L}(F_\theta(I + \delta, T), F_\theta(I, T))$, where \mathcal{L} measures the output discrepancy (e.g., cross-entropy or contrastive loss). **Encoder-based attacks** instead optimize δ by disrupting intermediate visual representations extracted by a surrogate encoder f_ϕ [10, 13, 53, 56, 77]:

$$\max_{\|\delta\|_p \leq \epsilon} \mathcal{L}(f_\phi(I + \delta), f_\phi(I)), \quad (3)$$

where \mathcal{L} is typically a feature distance loss (e.g., cosine distance). Encoder-based attacks have recently become attractive because they avoid optimizing over the full LVLM and do not require access to the generated outputs, thus being computationally cheap [10].

2.3 Encoder-based Transferability

Building on the transferability concept studied in [11, 34, 64], we define encoder-based transferability at the instance level as follows.

Definition 2.1 (Encoder-based Transferability). Let the victim LVLM be $V := \{f_\phi^V, M_\psi^V, L_\tau^V\}$, and $S := f_\phi^S$ be a surrogate vision encoder. Given a normal instance consisting of an image I , a prompt T , and a label y , let $I + \delta$ be a perturbed image crafted against a surrogate vision encoder S . The *encoder-based transferability* \mathcal{T} from S to V at the instance (I, T, y) is defined as

$$\mathcal{T}(S \rightarrow V; I, T, y) = \mathbb{I}\left[L_\tau^V(M_\psi^V(f_\phi^V(I + \delta)), T) \neq y\right],$$

where $\mathbb{I}[\cdot]$ is the indicator function.

Based on the above definition, achieving encoder-based transferability in LVLMs requires satisfying two conditions. **① Cross-encoder transferability:** the perturbations δ crafted against a surrogate encoder f_ϕ^S must also alter the victim LVLM’s vision encoder f_ϕ^V , even when their architectures differ (e.g., patch size or pretraining data). **② Encoder-to-model transferability:** once the perturbation δ has successfully transferred to the victim encoder f_ϕ^V , the resulting representation must further propagate through the alignment and language generation modules of the victim LVLM to ultimately alter its output. These two sub-conditions jointly determine the practical transferability of encoder-based attacks across the full LVLM inference.

2.4 Threat Model

We consider a zero-query black-box threat model for studying encoder-based transferability in LVLMs.

Adversary’s Knowledge. The adversary operates under a strict black-box setting, without access to any internal components of the victim LVLM, including its architecture, parameters, vision encoder, or output probabilities. Instead, the adversary leverages a publicly available vision–language pre-trained model (e.g., CLIP) that comprises a vision encoder $f_v(\cdot)$ and a text encoder $f_t(\cdot)$ jointly trained to align image–text pairs in a shared d -dimensional embedding space. For clarity, we denote $f_v(\cdot)$ as the surrogate vision encoder $f_\phi^S(\cdot)$ in line with our earlier Definition 2.1.

Adversary’s Capabilities. The adversary crafts adversarial examples solely using the surrogate model, without issuing any queries to the victim LVLM. These examples are then directly applied to the victim model, following the transfer-based attack paradigm. In contrast to query-based attacks, which rely on repeated interactions with the victim model to approximate gradients, this setting eliminates such dependencies, reflecting a more realistic scenario. We provide detailed attack scenarios with a case study in Appendix D.

3 Benchmarking Attack Transferability

Existing encoder-based LVLM attacks are mostly evaluated when surrogate and victim share identical (or closely related) encoders [10, 56, 66]. Such settings overestimate transferability and overlook the realistic case where encoders and language backbones differ. We therefore benchmark representative attacks on six open-source and two commercial LVLMs spanning diverse multimodal architectures.

3.1 Evaluation Setup

Surrogate and Victim Models. For the surrogate model, we adopt the widely used CLIP ViT-L/14 for all encoder-based attacks [56, 77], while BLIP-2 serves as the surrogate model for end-to-end attacks. For victim models, we select several representative LVLMs with diverse visual encoders.

Evaluation Attacks. We evaluate four representative untargeted attacks on LVLMs, including one end-to-end attack (Schlarmann and Hein [48]) and three encoder-based attacks (Cui et al. [10], Attack-Bard [13] and VT-Attack [56]).

Dataset and Setting. We evaluate image captioning using the prompt “Describe the image in one sentence.” We randomly sample 1,000 images from the Flickr30k [69] and generate adversarial examples under an ℓ_∞ budget of $\epsilon = 8/255$. Following prior work [54, 56, 77], we adopt projected gradient descent (PGD) with $K = 100$ iterations and step size $\alpha = 1/255$.

Evaluation Metric. To enable scalable and consistent evaluation while aligning with human judgment, we adopt an *LVLM-as-a-judge* protocol [66]. We employ a powerful LVLM GPT-4.1 with the following prompt and a clean image to verify whether the adversarial output remains a correct description of the image.

We provide detailed experimental setups in Appendix G.

3.2 Evaluation Results

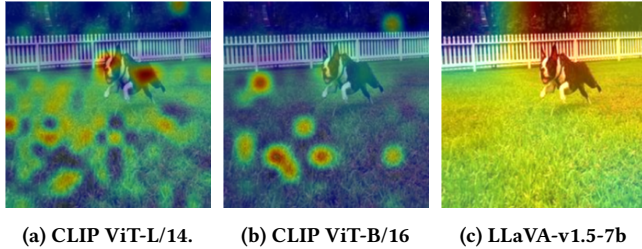
Table 1 reports the ASRs of four representative attacks against eight LVLMs. We first note that the end-to-end attack [48] achieves a pretty high ASR on its surrogate model (BLIP-2, 84.4%) but transfers poorly to other LVLMs, highlighting its limited utility in black-box scenarios. As a lightweight alternative, encoder-based attacks perturb only the vision encoder, and the state-of-the-art VT-Attack [56] achieves better transferability, outperforming the end-to-end baseline on all black-box victim models. Nevertheless, Table 1 also shows that encoder-based transferability remains limited overall, especially against advanced LVLMs such as GPT-4o and Gemini 2.0 Flash (ASR $\leq 11.0\%$). In particular, two phenomena stand out, illustrating how different components of LVLMs affect transferability.

Finding 1: Heterogeneous vision encoders limit encoder-based transferability. When the vision encoder of the victim LVLM matches the surrogate encoder, cross-encoder transferability is maximized, leading to strong encoder-based transferability. For example, OpenFlamingo, which shares the surrogate vision encoder, is nearly fully compromised (ASR $\approx 99.8\%$) under VT-Attack. In contrast, victim LVLMs with different encoders, such as Qwen2.5-VL, show substantially lower ASR, demonstrating that heterogeneous encoders inherently weaken encoder-based transferability.

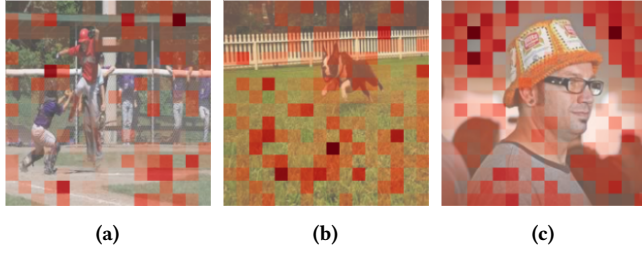
Finding 2: Advanced language modules further limit encoder-based transferability. Even with high cross-encoder transferability, overall encoder-based transferability can still be constrained by encoder-to-model transferability. For example, LLaVA shares the same vision encoder with the surrogate, like OpenFlamingo, yet records only 46% ASR under VT-Attack. This is possibly because its stronger LLaMA-2-7B backbone provides greater language understanding and robustness than OpenFlamingo’s OPT-2.7B, thereby diminishing the effect of visual perturbations. When both factors, heterogeneous encoders and advanced language modules, co-occur, such as in InternVL3, ASR drops even further ($\leq 32\%$).

Table 1: Attack success rate (ASR, %) of current attacks on LVLMs.

Attack	LLaVA	Qwen2.5-VL	InternVL3	OpenFlamingo	BLIP-2	Kimi-VL	GPT-4o	Gemini 2.0
Schlarmann and Hein [48]	28.4	26.8	23.0	59.4	84.4	23.2	8.4	5.4
Cui et al. [10]	41.8	24.2	24.6	97.0	26.8	21.8	7.0	5.6
Attack-Bard [13]	38.4	25.0	24.2	97.8	26.0	23.0	6.9	6.8
VT-Attack [56]	46.0	31.4	31.6	99.8	27.6	28.2	11.0	7.6



(a) CLIP ViT-L/14. (b) CLIP ViT-B/16. (c) LLaVA-v1.5-7b

Figure 1: Attention maps for the same input image showing differences in visual grounding across models.

(a) (b) (c)

Figure 2: Patch-level heatmaps for adversarial examples from VT-Attack [56]. Each red overlay denotes the cosine distance between patch embeddings of clean and adversarial images, with deeper red indicating larger feature deviations.

Summary. Existing attacks exhibit limited encoder-based transferability across diverse LVLMs. Their effectiveness is restricted by heterogeneous vision encoders (reducing *cross-encoder transferability*) and by advanced language modules (reducing *encoder-to-model transferability*), ultimately leading to lower overall transferability.

4 Transferability Analysis

In this section, we analyze why encoder-based attacks transfer poorly across heterogeneous LVLMs, using attention visualizations and patch-level perturbation heatmaps to identify two root causes and their failure patterns.

Root Cause 1: Inconsistent Visual Grounding Across Models.

Figure 1 illustrates this issue with attention maps from two CLIP encoders and one LLaVA model, revealing inconsistencies at two levels. (1) **Between vision encoders.** By comparing Figure 1a and Figure 1b, we observe that different encoders ground semantics in distinct regions: one distributes attention more broadly with multiple prominent activation regions, whereas the other concentrates attention more selectively on fewer focal areas. This inconsistency undermines *cross-encoder transferability*, since perturbations crafted on one encoder’s focus regions may not transfer to another. (2) **Between the visual encoder and the LVLM during generation.**

**Figure 3: Cross-attention map from LLaVA-v1.5-7b with masked images.**

By comparing Figures 1a and 1c, we find that even with the same encoder backbone, the cross-attention in LLaVA during text generation emphasizes regions different from those highlighted by the vision encoder. This indicates that the regions attended by the encoder are not necessarily the key evidence ultimately relied upon by the LLM for generation. This misalignment reduces *encoder-to-model transferability*, as perturbed visual features may not align with the features ultimately leveraged for text generation. Together, these two-level grounding inconsistencies hinder perturbations from propagating across different encoders and language modules, posing a major obstacle to transferability.

To further investigate how this obstacle affects attacks in practice, we analyze VT-Attack [56] and visualize patch-level perturbation heatmaps between clean and adversarial images in Figure 2. These visualizations reveal how perturbations are spatially distributed and allow us to identify recurring failure patterns that directly reflect the root cause. We can observe that **many perturbations are concentrated on visually salient but semantically irrelevant background areas**. For example, in Figure 2c, most perturbations fall on the background rather than on the person’s face. Compared to semantically stable foreground regions, such background-focused perturbations are highly inconsistent across encoders and largely ignored by the LVLM during generation, making them ineffective for altering the final output. This concrete failure pattern illustrates how the root cause manifests in practice: perturbations optimized on one encoder often collapse onto unstable background regions that neither transfer reliably nor influence generation.

Root Cause 2: Redundant Semantic Alignment Within Models.

Beyond inconsistent visual grounding, LVLMs also exhibit redundant semantic alignment that further complicates attack transferability. Unlike unimodal encoders that typically condense information into a single representation, LVLMs propagate features from multiple image patches into the language model. This design creates overlapping pathways where each semantic concept can be redundantly supported by multiple visual tokens [33, 68]. As shown in Figure 3, even when we mask out the majority of the dog in the image, the cross-attention distribution remains largely

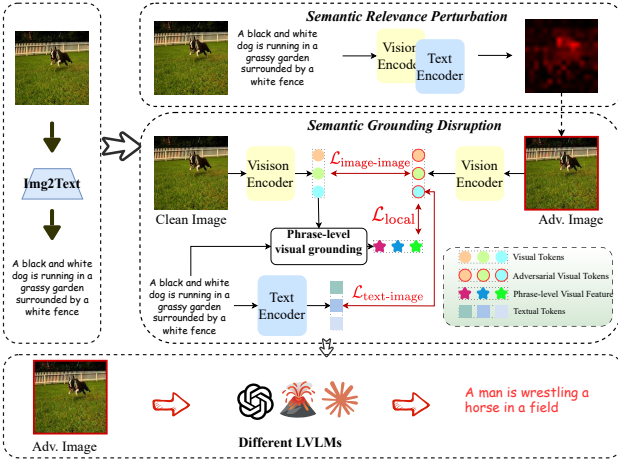


Figure 4: The framework of SGMA.

unchanged and the model still correctly recognizes the object as a dog. This indicates that a small subset of patches (e.g., a leg or an ear) can already trigger the “dog” label, revealing the semantic redundancy across patches. This redundancy reduces the *encoder-to-model transferability*, as effective attacks would need to disrupt most or all evidence-carrying patches.

We can also observe the failure patterns corresponding to this root cause in Figure 2: **perturbations within semantic regions are often too weak or scattered to cover all critical patches, leaving large parts of the object intact**. These remaining clean patches still provide sufficient redundant evidence for recognition. As shown in Figure 2b, the attack perturbs only a few patches on the dog, leaving large portions of its body intact, while in Figure 2c, perturbations around the person’s face are dispersed and miss key features such as the eyes and mouth. Since LVLMs redundantly encode semantic concepts across multiple tokens, as long as some evidence-carrying patches remain unperturbed, the models can still rely on them for correct recognition, causing the attack to have little effect on the final output.

5 Semantic-Guided Multimodal Attack

5.1 Overview

Building on the previous analysis, we propose **Semantic-Guided Multimodal Attack (SGMA)**, a framework explicitly designed to mitigate the above-mentioned root causes that limit the transferability of encoder-based attacks. Motivated by the failure patterns of existing attacks, our core idea is to (i) direct perturbations toward semantically meaningful foreground regions that remain consistent across models, and (ii) increase their density and strength within these regions so that the perturbations cannot be easily bypassed by the redundant tokens in LVLMs. As shown in Figure 4, SGMA consists of the following two components.

(1) To mitigate root cause 1, we propose a **Semantic Relevance Perturbation** strategy that directs perturbations toward semantically meaningful regions while suppressing inconsistent background areas. Specifically, we generate a soft mask by mapping

the paired description onto visual patches with high semantic relevance, which is then used to modulate perturbation magnitudes. This ensures that perturbations concentrate on regions that remain consistently important across models.

(2) To mitigate root cause 2, we propose a **Semantic Grounding Disruption** strategy that increases the density of perturbations within semantically relevant regions. We design a multi-level objective that imposes semantic disruption at both the global and local levels. At the global level, the adversarial image is pushed away from its clean counterpart and paired caption in the aligned embedding space. At the local level, perturbations are enforced consistently across all patches associated with the same noun phrase, ensuring that entire semantic concepts are disrupted rather than only a few isolated patches.

5.2 Semantic Relevance Perturbation

Prior studies have shown that vision encoders trained on large-scale image–text pairs tend to prioritize semantically meaningful regions aligned with textual descriptions, as these areas receive repeated emphasis during contrastive learning [29, 44]. Similarly, LVLMs rely on these regions to support reasoning and generation [24, 32, 78]. These findings suggest that perturbations on foreground regions are inherently more transferable than those on background areas.

Motivated by this, we explicitly guide adversarial perturbations toward semantically important regions to enhance overall transferability. To achieve this, we adopt Grad-ECLIP [76], which provides fine-grained localization of text-aligned visual tokens in CLIP. Unlike gradient- or attention-based techniques applied directly to encoders (e.g., Grad-CAM [49], attention rollout [3]), which often introduce unacceptable model-specific biases [30, 58], Grad-ECLIP leverages the text embedding as an anchor to constrain gradients, enabling cross-modal localization of semantically aligned regions. Although these regions may not perfectly match the important semantic areas of other LVLMs, CLIP’s large-scale pretraining on diverse image–text pairs ensures they serve as a relatively stable proxy for transferable perturbation targets. Concretely, the semantic relevance perturbation includes the following steps.

Step 1: Semantic Reference Generation. We first query a pre-trained LVLM (e.g., GPT-4o or LLaVA) to summarize the image I into a concise caption T_d . This summary T_d captures the model’s semantic understanding of the image and serves as a natural reference for grounding. By aligning I with T_d , we can highlight the visual regions contributing most to that semantic content. Note that both open- and closed-source LVLMs produce comparable captions for this step and similar attack performance, since caption generation here only requires coarse-grained semantics where the models yield highly consistent outputs.

Step 2: Semantic Relevance Localization. We then leverage Grad-ECLIP to derive a text-conditioned patch-level attention map A for I . Given the normalized image and text embeddings $v = f_v(I)$ and $t = f_t(T_d)$, we compute their cosine similarity $\mathcal{L}_{\cos} = v^\top t$ and backpropagate it to obtain the gradient $\nabla_{o_{\text{CLS}}} \mathcal{L}_{\cos}$ with respect to the [CLS] token output o_{CLS} . Let $v_i \in \mathbb{R}^{d_v}$ denote the value vector of the i -th image patch token in the final transformer layer (where d_v is the vision encoder’s hidden dimension), and α_i the averaged attention weight assigned to patch i by the [CLS] token across all

attention heads. The saliency score for patch i is then calculated as $s_i = \alpha_i \cdot (\mathbf{v}_i \cdot \nabla_{\text{CLS}} \mathcal{L}_{\text{cos}})$, which reflects the patch's contribution to the similarity, modulated by both attention and gradient relevance.

The patch-level scores $\{s_i\}_{i=1}^{HW}$ (with $H \times W$ denoting the patch grid size) are then reshaped into a 2D spatial map $\mathbf{A} \in \mathbb{R}^{H \times W}$ and bilinearly upsampled to the input resolution $R \times R$, yielding a pixel-level semantic mask $\mathbb{M} \in [0, 1]^{R \times R}$. This map captures the patch-level gradient attribution of visual features with respect to the semantic text prompt and serves as a semantic relevance mask for perturbation localization.

Step 3: Perturbation Allocation. Finally, we employ \mathbb{M} to generate a pixel-wise perturbation map $\epsilon_{\text{map}} \in \mathbb{R}^{R \times R}$ under a global perturbation budget constraint, where the total perturbation budget is bounded while allowing adaptive allocation across pixels. We define $\epsilon > 0$ as the average per-pixel perturbation budget and $r \in [0, 1]$ as the base ratio controlling the trade-off between uniform and focused allocation. The allocation is formulated as:

$$\epsilon_{\text{map}}(i, j) = \epsilon_{\text{bg}} + \frac{\mathbb{M}(i, j)}{\sum_{x=1}^R \sum_{y=1}^R \mathbb{M}(x, y)} \cdot \epsilon_{\text{fg, total}}, \quad (4)$$

where $\epsilon_{\text{bg}} = r \cdot \epsilon$ is a uniform base perturbation assigned to every pixel, and $\epsilon_{\text{fg, total}} = \epsilon \cdot (1 - r) \cdot R^2$ is the remaining budget for focused allocation to semantically important regions. This formulation ensures that the total perturbation budget across all pixels equals $\epsilon \cdot R^2$, while regions with higher semantic importance scores receive stronger perturbations.

5.3 Semantic Grounding Disruption

While semantic relevance perturbation improves transferability by guiding perturbations toward semantically important regions, it does not ensure that these regions are perturbed with sufficient density and strength to overcome redundancy. This limitation highlights the need for explicitly reinforcing semantic disruption in the optimization objective.

To this end, we introduce *semantic grounding disruption*, a dual-faceted strategy that weakens semantic alignment at two complementary levels. (1) **Global semantic disruption** induces large-scale shifts in overall visual semantics, reducing alignment with the textual description and distorting the image representation. (2) **Local semantic disruption** targets region–phrase correspondences by perturbing the set of visual tokens associated with each noun phrase, ensuring that key semantic concepts are consistently disrupted rather than only a few isolated patches. By jointly applying these two levels, our method amplifies the disruption of semantic grounding, achieving stronger and denser perturbations that lead to a more comprehensive degradation of multimodal understanding.

5.3.1 Global Semantic Disruption. The objective of *global semantic disruption* is twofold: (1) disrupting the alignment between the image and its original textual description T_d in the joint vision–language embedding space; and (2) inducing a substantial shift in the overall visual semantics, making the adversarial image I_{adv} semantically distinct from the original clean image I . They are realized with the following two loss terms.

(1) Text–Image Loss. This loss measures the cosine distance between I_{adv} and T_d in the aligned embedding space to disrupt their

global semantic alignment. It is formulated as:

$$\mathcal{L}_{\text{text-image}}(I_{\text{adv}}, T_d) = 1 - \cos(f_v(I_{\text{adv}}), f_t(T_d)), \quad (5)$$

where $\cos(\cdot, \cdot)$ denotes the cosine similarity. By maximizing this loss, we encourage the adversarial image to be semantically misaligned with its original textual description.

(2) Image–Image Loss. This loss measures the cosine distance between I_{adv} and the original image I . Let $f_v^{\text{all}}(\cdot) \in \mathbb{R}^{(HW+1) \times d_v}$ denote all visual tokens from the vision encoder (including both [CLS] and $H \times W$ patch tokens) before projection. The loss is:

$$\mathcal{L}_{\text{image-image}}(I_{\text{adv}}, I) = 1 - \cos(f_v^{\text{all}}(I_{\text{adv}}), f_v^{\text{all}}(I)). \quad (6)$$

Using all tokens, rather than only the [CLS] embedding or the projected vision features, can capture both coarse- and fine-grained visual semantics, ensuring that perturbations alter detailed features and overall representation. By maximizing this loss, we distort the holistic visual semantics of I_{adv} .

5.3.2 Local Semantic Disruption. Although global disruption weakens both cross-modal alignment (image–text) and unimodal consistency (image–image), it often fails to inject sufficient density and strength into specific semantic regions since it primarily encourages large shifts in the overall embedding space. To fully disrupt semantic understanding, we introduce *local semantic disruption*, which explicitly targets the set of visual tokens linked to each noun phrase. We restrict our focus to noun phrases because they provide stable visual anchors, while verbs usually rely on the visual evidence of associated objects (e.g., a person's mouth and food for “eating”), which is already captured through noun-based patches. By concentrating perturbations on these tokens, our method increases perturbation density within semantically coherent areas, thereby breaking redundant region–phrase grounding. We implement this in the following three steps.

Step 1: Noun Phrase Extraction. Given a textual description T_d , we extract N noun phrases $\{p_n\}_{n=1}^N$ using the SpaCy en_core_web_sm model [16], which detects all noun chunks. We remove duplicates and stop words to ensure clean phrase sets. Here, $N \geq 1$ in all cases due to the presence of at least one noun phrase.

Step 2: Phrase–Token Association. For each p_n , we compute a CLIP-based patch relevance map $\mathbf{A}_n \in \mathbb{R}^{H \times W}$ using the same Grad-ECLIP procedure from Section 5.2, with p_n as the text input instead of T_d . Let $\mathbf{A}_n^{\text{flat}} \in \mathbb{R}^{HW \times 1}$ be its flattened version. The set of relevant visual token indices is:

$$\mathcal{R}_n = \{i \in [0, HW) \mid \mathbf{A}_n^{\text{flat}}[i] > \tau\}, \quad (7)$$

where $\tau \in (0, 1)$ is a fixed relevance threshold chosen to balance coverage and precision. If \mathcal{R}_n is empty, the phrase is discarded from the loss computation.

Step 3: Local Semantic Loss. Let $f_v^{\text{patch}}(\cdot) \in \mathbb{R}^{HW \times d_v}$ denote the patch visual tokens (excluding [CLS]) from the final visual encoder layer. For each p_n , we compute its *phrase-level visual feature* $\mathbf{c}_n \in \mathbb{R}^{d_v}$ by averaging the normalized clean visual tokens over \mathcal{R}_n . To disrupt region–phrase correspondence at a fine-grained level, we define the local semantic loss as:

$$\mathcal{L}_{\text{local}}(I_{\text{adv}}, \mathcal{R}_n) = \frac{1}{N} \sum_{n=1}^N \frac{1}{|\mathcal{R}_n|} \sum_{i \in \mathcal{R}_n} \left[1 - \cos(f_v^{\text{patch}}(I_{\text{adv}})[i], \mathbf{c}_n) \right], \quad (8)$$

which penalizes similarity between adversarial visual tokens and the clean phrase-level visual feature, explicitly disrupting fine-grained region–phrase alignment and weakening localized multimodal understanding.

5.4 Overall Attack Process

Our final attack objective integrates the perturbation allocation strategy (*semantic relevance perturbation*) and the representation disruption strategy (*semantic grounding disruption*) into a unified optimization framework. Given a clean image I and its caption T_d , the adversarial image is $I_{\text{adv}} = I + \delta$, where δ is constrained by a pixel-wise budget ϵ_{map} . The total loss combines global and local grounding disruption:

$$\mathcal{L}_{\text{total}} = \mathcal{L}_{\text{text-image}} + \mathcal{L}_{\text{image-image}} + \mathcal{L}_{\text{local}}. \quad (9)$$

The optimization problem is:

$$\max_{\delta} \mathcal{L}_{\text{total}} \quad \text{s.t.} \quad |\delta(x, y)|_{\infty} \leq \epsilon_{\text{map}}(x, y), \quad \forall (x, y). \quad (10)$$

We solve this using PGD, iteratively updating δ in the gradient ascent direction and projecting it back to the ℓ_{∞} ball defined by ϵ_{map} . The overall algorithm is given in Algorithm 1 in Appendix.

6 Experiment

6.1 Experimental Setup

Surrogate and Victim Models. We employ the same set of victim models as detailed in Section 3.1. For surrogate models, we select CLIP-L/14 (default), CLIP-B/16, and SigLIP [70] to investigate the impact of surrogates. Additionally, we introduce an ensemble variant combining CLIP-L/14, CLIP-B/16, and CLIP-B/32, to assess the compatibility of SGMA with general transfer-enhancing strategies. **Datasets.** We randomly sample 1,000 samples from each of three datasets for evaluation, corresponding to different multimodal tasks: image captioning on Flickr30k [69] using the prompt “Describe the image in one sentence”, image classification on CIFAR-10 [26] using the prompt in Section G, and visual question answering (VQA) on the TextVQA validation set [52]. Diverse datasets cover both object-centric recognition and text-based reasoning scenarios.

Metrics. We use ASR to quantify attack effectiveness across all tasks, though the computation method varies depending on the task nature. For classification and VQA tasks, ASR is computed as the proportion of adversarial samples that induce incorrect model predictions compared to clean samples. For the captioning task, since there is no ground-truth “correct/incorrect” prediction, we use an *LVLM-as-a-Judge* approach (see Section 3.1). Additionally, following [56, 77], we report CLIP similarity for the captioning task to assess the alignment between adversarially generated text y_{adv} and the clean image I . Lower CLIP similarity values and higher ASR both indicate stronger attacks.

Baselines. We compare our proposed SGMA with four representative LVLM attacks [10, 13, 48, 56], as well as three transfer-based attacks originally designed for ViTs [61, 71]. Specifically, TGR [71] regularizes token gradients to reduce variance and concentrate perturbations on more transferable components, while PNA and PatchOut [61] improve transferability by treating attention weights

as constants and randomly masking patches during backpropagation. We adapt these transfer-based methods to the LVLM setting by integrating them into the framework of Cui et al. [10].

Attack Setting. For each image, we obtain a concise description T_d from GPT-4o using the prompt “Describe this image in a short sentence.” Perturbations are bounded by $\epsilon = 8/255$ under the ℓ_{∞} norm and optimized with PGD using $K = 100$ steps and step size $\alpha = 1/255$. We set the default values of base ratio $r = 0.2$ and relevance threshold $\tau = 0.3$.

6.2 Experimental Results

We evaluate the effectiveness of SGMA across eight popular LVLMs and compare it against several existing adversarial attacks, with the main results shown in Tables 2, 6 and 7. Furthermore, we assess the imperceptibility of generated adversarial examples in Appendix H.2, and provide visual illustrations in Appendix F to explain why SGMA achieves higher transferability. Overall, our results show that SGMA consistently reduces image–text CLIP similarity while achieving higher ASR, demonstrating superior transferability. We present further insights and discussions below.

❶ Transfer-enhancing strategies originally designed for ViTs, such as PNA [61], PatchOut [61], and TGR [71], show limited effectiveness in LVLMs. These methods mainly perturb the CLS token, which is effective in classification tasks where final predictions rely on this global representation, but ineffective in LVLMs that depend on fine-grained patch-level representations. In particular, PatchOut further weakens transferability by discarding patches, thereby reducing perturbation density on key regions instead of corrupting the redundant tokens that LVLMs depend on.

❷ Models with fewer parameters are generally more vulnerable to adversarial attacks. For instance, OpenFlamingo, with only 4 billion parameters, is nearly completely compromised, reaching an ASR of 99.8%. In contrast, closed-source models such as GPT-4o and Gemini, which are believed to contain hundreds of billions of parameters, exhibit significantly greater robustness, with ASR values reduced to approximately 20%.

❸ Commercial LVLMs present substantially higher resistance to attacks. While our method achieves higher ASR on open-source models (e.g., 64.0% on LLaVA), the ASR drops on commercial LVLMs like GPT-4o (25.2%) and Gemini 2.0 (18.2%). This suggests that closed-source APIs integrate more robust defense mechanisms, such as safety-aligned training, input detection, and purification, which are absent in open-source weights. Our findings call for future exploration of defense-aware attacks to further enhance attack performance. Despite the performance gap, these ASRs remain non-trivial given the zero-query black-box setting and reflect the strength of our attack even under real-world constraints.

Component Ablation of SGMA. Table 3 presents an ablation analysis of the proposed SGMA method on three LVLMs. We progressively introduce three key components: global semantic disruption, local semantic disruption, and semantic relevance perturbation. For the variant without semantic-relevance perturbation, the perturbation budget is distributed uniformly across all pixels. The results show that each component contributes to improving attack effectiveness. Notably, incorporating local semantic disruption on top of global semantic disruption yields a consistent improvement in ASR (e.g.,

Table 2: The attack performance on victim LVLMs, including both open-source and commercial models. Bold indicates the best performance. Results on more LVLMs and more tasks are provided in Appendix H.1 (Tables 6 and 7).

Victim LVLM	Attack	CLIP Similarity between image and generated text ↓						ASR (%) ↑
		RN-50	RN-101	ViT-B/16	ViT-B/32	ViT-L/14	Ensemble	
LLaVA	Clean	0.2421	0.4646	0.3061	0.2988	0.2637	0.3151	-
	TGR [71]	0.2364	0.4577	0.2986	0.2935	0.2527	0.3078	35.6
	PNA [61]	0.2417	0.4639	0.3049	0.2998	0.2616	0.3144	22.6
	PNA + PathOut [61]	0.2427	0.4642	0.3063	0.3001	0.2633	0.3153	17.6
	Cui et al. [10]	0.2365	0.4584	0.2981	0.2925	0.2530	0.3077	41.8
	Schlarmann and Hein [48]	0.2376	0.4600	0.3011	0.2946	0.2563	0.3099	28.4
	Attack-Bard [13]	0.2354	0.4568	0.2964	0.2915	0.2498	0.3060	38.4
	VT-Attack [56]	0.2330	0.4544	0.2939	0.2892	0.2462	0.3033	46.0
	SGMA	0.2282	0.4493	0.2873	0.2831	0.2376	0.2971	55.4
	Clean	0.2578	0.4843	0.3197	0.3130	0.2702	0.3290	-
Qwen2.5-VL	TGR [71]	0.2546	0.4802	0.3149	0.3095	0.2624	0.3243	24.0
	PNA [61]	0.2533	0.4787	0.3131	0.3080	0.2623	0.3231	22.6
	PNA + PathOut [61]	0.2554	0.4810	0.3159	0.3103	0.2660	0.3257	19.0
	Cui et al. [10]	0.2530	0.4789	0.3135	0.3079	0.2620	0.3231	24.2
	Schlarmann and Hein [48]	0.2523	0.4783	0.3134	0.3075	0.2619	0.3227	26.8
	Attack-Bard [13]	0.2524	0.4788	0.3129	0.3066	0.2607	0.3223	25.0
	VT-Attack [56]	0.2497	0.4762	0.3105	0.3052	0.2571	0.3197	31.4
	SGMA	0.2481	0.4738	0.3070	0.3019	0.2540	0.3169	39.0
	Clean	0.2575	0.4861	0.3228	0.3132	0.2798	0.3319	-
	TGR [71]	0.2547	0.4833	0.3191	0.3120	0.2740	0.3286	8.2
GPT-4o	PNA [61]	0.2574	0.4857	0.3200	0.3145	0.2780	0.3311	6.4
	PNA + PathOut [61]	0.2590	0.4873	0.3231	0.3168	0.2796	0.3332	3.8
	Cui et al. [10]	0.2551	0.4839	0.3197	0.3130	0.2759	0.3295	7.0
	Schlarmann and Hein [48]	0.2561	0.4844	0.3207	0.3118	0.2755	0.3297	8.4
	Attack-Bard [13]	0.2571	0.4846	0.3196	0.3121	0.2741	0.3295	6.9
	VT-Attack [56]	0.2556	0.4833	0.3187	0.3109	0.2727	0.3283	11.0
	SGMA	0.2535	0.4815	0.3151	0.3085	0.2681	0.3253	16.6
	Clean	0.2588	0.4841	0.3230	0.3162	0.2828	0.3330	-
	TGR [71]	0.2617	0.4893	0.3258	0.3174	0.2816	0.3352	7.6
	PNA [61]	0.2612	0.4880	0.3243	0.3160	0.2808	0.3341	5.2
Gemini 2.0	PNA + PathOut [61]	0.2606	0.4875	0.3240	0.3161	0.2808	0.3338	5.4
	Cui et al. [10]	0.2564	0.4813	0.3187	0.3119	0.2792	0.3295	5.6
	Schlarmann and Hein [48]	0.2539	0.4808	0.3185	0.3112	0.2760	0.3281	5.4
	Attack-Bard [13]	0.2562	0.4819	0.3197	0.3117	0.2764	0.3292	6.8
	VT-Attack [56]	0.2547	0.4809	0.3178	0.3108	0.2758	0.3280	7.6
	SGMA	0.2527	0.4781	0.3150	0.3082	0.2714	0.3251	13.2

Table 3: Component ablation of SGMA. ✓_{II} = Global disruption with only image–image loss.

Victim LVLM	Method			CLIP Similarity between image and generated text (↓)						ASR (%) (↑)
	Global disrupt.	Local disrupt.	Semantic pert.	RN-50	RN-101	ViT-B/16	ViT-B/32	ViT-L/14	Ensemble	
LLaVA	✓ _{II}			0.2377	0.4590	0.2988	0.2945	0.2530	0.3086	39.0
	✓			0.2324	0.4547	0.2935	0.2885	0.2459	0.3030	44.2
	✓	✓		0.2354	0.4564	0.2971	0.2909	0.2502	0.3060	48.8
	✓	✓	✓	0.2302	0.4495	0.2880	0.2846	0.2369	0.2978	55.4
Qwen2.5-VL	✓ _{II}			0.2536	0.4786	0.3143	0.3090	0.2620	0.3235	25.0
	✓			0.2528	0.4766	0.3117	0.3063	0.2603	0.3215	30.0
	✓	✓		0.2512	0.4772	0.3117	0.3062	0.2586	0.3209	31.2
	✓	✓	✓	0.2468	0.4732	0.3052	0.3014	0.2516	0.3156	39.0
InternVL3	✓ _{II}			0.2553	0.4804	0.3156	0.3108	0.2676	0.3260	23.5
	✓			0.2507	0.4774	0.3119	0.3055	0.2632	0.3217	28.7
	✓	✓		0.2511	0.4770	0.3102	0.3059	0.2621	0.3213	35.4
	✓	✓	✓	0.2462	0.4718	0.3052	0.3013	0.2559	0.3161	41.2

44.2% \rightarrow 48.8% for LLaVA), while the introduction of semantic relevance perturbation further boosts ASR significantly (e.g., up to 55.4% for LLaVA).

Due to space limitations, we include additional analyses in Appendix H.3, covering the effects of surrogate models, perturbation budget ϵ , base ratio r , relevance threshold τ , the number of attack steps, and computational cost. We further discuss potential defenses, model-ensemble settings, targeted-attack extensions, and limitations in Appendix I.

7 Conclusion

In this paper, we present the first systematic study of encoder-based transferability against LVLMs in zero-query black-box settings. We show that existing adversarial attacks suffer from poor transferability, primarily due to two root causes: inconsistent visual grounding across models and redundant semantic alignment within models. Motivated by these insights, we propose SGMA, a semantic-guided multimodal attack framework that reallocates perturbations to semantically stable regions and disrupts cross-modal alignment at both global and local levels. Extensive experiments across diverse LVLMs and tasks demonstrate that SGMA substantially improves transferability while preserving visual imperceptibility. This study advances our understanding of encoder-based adversarial transferability in LVLMs, and highlights actionable directions for designing stronger encoder-based attacks and developing effective defenses for multimodal systems.

References

[1] [n. d.]. Cat and Dog Dataset. <https://www.kaggle.com/datasets/tongpython/cat-and-dog>. Accessed: 2025-07-22.

[2] [n. d.]. COVID-19 Radiography Database. <https://www.kaggle.com/datasets/tawsifurrahman/covid19-radiography-database>. Accessed: 2025-08-25.

[3] Samira Abnar and Willem Zuidema. 2020. Quantifying Attention Flow in Transformers. In *ACL*.

[4] Jean-Baptiste Alayrac, Jeff Donahue, Pauline Luc, Antoine Miech, Iain Barr, Yana Hasson, Karel Lenc, Arthur Mensch, Katherine Millican, Malcolm Reynolds, et al. 2022. Flamingo: A Visual Language Model for Few-Shot Learning. In *NeurIPS*.

[5] Bakary Badjie, José Cecílio, and Antonio Casimiro. 2024. Adversarial Attacks and Countermeasures on Image Classification-based Deep Learning Models in Autonomous Driving Systems: A Systematic Review. *ACM Comput. Surv.* (Oct. 2024).

[6] Nicholas Carlini, Anish Athalye, Nicolas Papernot, Wieland Brendel, Jonas Rauber, Dimitris Tsipras, Ian Goodfellow, Aleksander Madry, and Alexey Kurakin. 2019. On evaluating adversarial robustness. *arXiv preprint arXiv:1902.06705* (2019).

[7] Dongping Chen, Ruoxi Chen, Shilin Zhang, Yaochen Wang, Yinuo Liu, Huichi Zhou, Qihui Zhang, Yao Wan, Pan Zhou, and Lichao Sun. 2024. MLLM-as-a-Judge: assessing multimodal LLM-as-a-Judge with vision-language benchmark. In *ICML*.

[8] Kai Chen, Yanze Li, Wenhua Zhang, Yanxin Liu, Pengxiang Li, Ruiyuan Gao, Lanqing Hong, Meng Tian, Xinhai Zhao, Zhenguo Li, et al. 2025. Automated Evaluation of Large Vision-Language Models on Self-Driving Corner Cases. In *WACV*.

[9] Zhe Chen, Jiannan Wu, Wenhui Wang, Weijie Su, Guo Chen, Sen Xing, Muyan Zhong, Qinglong Zhang, Xizhou Zhu, Lewei Lu, et al. 2024. InternVL: Scaling up Vision Foundation Models and Aligning for Generic Visual-Linguistic Tasks. In *CVPR*.

[10] Xuanning Cui, Alejandro Aparcedo, Young Kyun Jang, and Ser-Nam Lim. 2024. On the Robustness of Large Multimodal Models Against Image Adversarial Attacks. In *CVPR*.

[11] Ambra Demontis, Marco Melis, Maura Pintor, Matthew Jagielski, Battista Biggio, Alina Oprea, Cristina Nita-Rotaru, and Fabio Roli. 2019. Why Do Adversarial Attacks Transfer? Explaining Transferability of Evasion and Poisoning Attacks. In *USENIX Security*.

[12] Junhao Dong, Piotr Koniusz, Xinghua Qu, and Yew-Soon Ong. 2025. Stabilizing modality gap & lowering gradient norms improve zero-shot adversarial robustness of vlms. In *Proceedings of the 31st ACM SIGKDD Conference on Knowledge Discovery and Data Mining V. 1*.

[13] Yinpeng Dong, Huanran Chen, Jiawei Chen, Zhengwei Fang, Xiao Yang, Yichi Zhang, Yu Tian, Hang Su, and Jun Zhu. 2023. How Robust Is Google’s Bard to Adversarial Image Attacks? *arXiv preprint arXiv:2309.11751* (2023).

[14] Yinpeng Dong, Fangzhou Liao, Tianyu Pang, Hang Su, Jun Zhu, Xiaolin Hu, and Jianguo Li. 2018. Boosting Adversarial Attacks with Momentum. In *CVPR*.

[15] Yinpeng Dong, Tianyu Pang, Hang Su, and Jun Zhu. 2019. Evading defenses to transferable adversarial examples by translation-invariant attacks. In *CVPR*.

[16] Explosion. 2025. spaCy en_core_web_sm (v3.7.1). https://huggingface.co/spacy/en_core_web_sm.

[17] L. John Fahrner, Emma Chen, Eric Topol, and Pranav Rajpurkar. 2025. The Generative Era of Medical AI. *Cell* (2025).

[18] Yuxin Fang, Wen Wang, Binhuai Xie, Quan Sun, Ledell Wu, Xinggang Wang, Tiejun Huang, Xinlong Wang, and Yue Cao. 2023. EVA: Exploring the Limits of Masked Visual Representation Learning at Scale. In *CVPR*.

[19] Zhe Gan, Yen-Chun Chen, Linjie Li, Chen Zhu, Yu Cheng, and Jingjing Liu. 2020. Large-Scale Adversarial Training for Vision-and-Language Representation Learning. In *NeurIPS*.

[20] Gemini Team, Rohan Anil, Sebastian Borgeaud, Jean-Baptiste Alayrac, Jiahui Yu, Radu Soricut, Johan Schalkwyk, Andrew M Dai, Anja Hauth, Katie Millican, et al. 2023. Gemini: A Family of Highly Capable Multimodal Models. *arXiv preprint arXiv:2312.11805* (2023).

[21] Chuan Guo, Mayank Rana, Moustapha Cissé, and Laurens van der Maaten. 2018. Countering Adversarial Images using Input Transformations. In *ICLR*.

[22] Xiao Han, Chen Zhu, Hengshu Zhu, and Xiangyu Zhao. 2025. Swarm intelligence in geo-localization: A multi-agent large vision-language model collaborative framework. In *Proceedings of the 31st ACM SIGKDD Conference on Knowledge Discovery and Data Mining V. 2*.

[23] Yutao Hu, Tianbin Li, Quanfeng Lu, Wenqi Shao, Junjun He, Yu Qiao, and Ping Luo. 2024. OmniMedVQA: A New Large-Scale Comprehensive Evaluation Benchmark for Medical LVLML. In *CVPR*.

[24] Seil Kang, Jinyeong Kim, Junhyeok Kim, and Seong Jae Hwang. 2025. See What You Are Told: Visual Attention Sink in Large Multimodal Models. In *ICLR*.

[25] Kimi Team, Angang Du, Bohong Yin, Bowei Xing, Bowen Qu, et al. 2025. Kimi-VL Technical Report. *arXiv preprint arXiv:2504.07491* (2025).

[26] Alex Krizhevsky. 2009. *Learning Multiple Layers of Features from Tiny Images*. Technical Report. University of Toronto.

[27] Huiying Li, Shawn Shan, Emily Wenger, Jiayun Zhang, Haitao Zheng, and Ben Y. Zhao. 2022. Blacklight: Scalable Defense for Neural Networks against Query-Based Black-Box Attacks. In *USENIX Security*.

[28] Junnan Li, Dongxu Li, Silvio Savarese, and Steven Hoi. 2023. BLIP-2: Bootstrapping Language-Image Pre-training with Frozen Image Encoders and Large Language Models. In *ICML*.

[29] Junnan Li, Ramprasaath Selvaraju, Akhilesh Gotmare, Shafiq Joty, Caiming Xiong, and Steven Chu Hong Hoi. 2021. Align before Fuse: Vision and Language Representation Learning with Momentum Distillation. In *NeurIPS*.

[30] Zhiwei Li, Min Ren, Qi Li, Fangling Jiang, and Zhenan Sun. 2024. Improving Transferability of Adversarial Samples via Critical Region-Oriented Feature-Level Attack. *IEEE Transactions on Information Forensics and Security* (2024).

[31] Tianwei Lin, Wenqiao Zhang, Sijing Li, Yuqian Yuan, Binhe Yu, Haoyuan Li, Wanggui He, Hao Jiang, Mengze Li, Xiaohui Song, Siliang Tang, Jun Xiao, Hui Lin, Yueteng Zhuang, and Beng Chin Ooi. 2025. HealthGPT: A Medical Large Vision-Language Model for Unifying Comprehension and Generation via Heterogeneous Knowledge Adaptation. In *ICML*.

[32] Haotian Liu, Chunyan Li, Qingshang Wu, and Yong Jae Lee. 2023. Visual Instruction Tuning. In *NeurIPS*.

[33] Ting Liu, Liangtao Shi, Richang Hong, Yue Hu, Quanjun Yin, and Linfeng Zhang. 2024. Multi-stage Vision Token Dropping: Towards Efficient Multimodal Large Language Model. *arXiv preprint arXiv:2411.10803* (2024).

[34] Yanpei Liu, Xinyun Chen, Chang Liu, and Dawn Song. 2017. Delving into Transferable Adversarial Examples and Black-box Attacks. In *ICLR*.

[35] Jannik Lübbertedt, Esteban Rivera Guerrero, Nico Uhlemann, and Markus Lienkamp. 2025. V3LMA: Visual 3D-Enhanced Language Model for Autonomous Driving. In *CVPR*.

[36] Yisroel Mirsky, Tom Mahler, Ilan Shelef, and Yuval Elovici. 2019. CT-GAN: Malicious Tampering of 3D Medical Imagery using Deep Learning. In *USENIX Security*.

[37] Muzammal Naseer, Salman Khan, Munawar Hayat, Fahad Shahbaz Khan, and Fatih Porikli. 2020. A Self-supervised Approach for Adversarial Robustness. In *CVPR*.

[38] Vishwesh Nath, Wenqi Li, Dong Yang, Andriy Myronenko, Mingxin Zheng, Yao Lu, Zhijian Liu, Hongxu Yin, Yee Man Law, Yucheng Tang, et al. 2025. VILA-M3: Enhancing Vision-Language Models with Medical Expert Knowledge. In *CVPR*.

[39] Weili Nie, Brandon Guo, Yujia Huang, Chaowei Xiao, Arash Vahdat, and Anima Anandkumar. 2022. Diffusion Models for Adversarial Purification. In *ICML*.

[40] OpenAI. 2025. Introducing GPT-4.5. <https://openai.com/index/introducing-gpt-4-5>.

[41] OpenAI, Josh Achiam, Steven Adler, Sandhini Agarwal, et al. 2024. GPT-4 Technical Report. *arXiv preprint arXiv:2303.08774* (2024).

[42] Jielin Qiu, Yi Zhu, Xingjian Shi, Zhiqiang Tang, Ding Zhao, Bo Li, and Mu Li. 2022. Benchmarking Robustness under Distribution Shift of Multimodal Image-Text Models. In *NeurIPS 2022 Workshop on Distribution Shifts: Connecting Methods and Applications*.

[43] Qwen Team. 2025. Qwen2.5 VL! Qwen2.5 VL! Qwen2.5 VL! <https://qwen.ai/blog?id=qwen2.5-vl>.

[44] Alec Radford, Jong Wook Kim, Chris Hallacy, Aditya Ramesh, Gabriel Goh, Sandhini Agarwal, Girish Sastry, Amanda Askell, Pamela Mishkin, Jack Clark, et al. 2021. Learning Transferable Visual Models From Natural Language Supervision. In *ICML*.

[45] Vishwanatha M Rao, Michael Hla, Michael Moor, Subathra Adithan, Stephen Kwak, Eric J Topol, and Pranav Rajpurkar. 2025. Multimodal Generative AI for Medical Image Interpretation. *Nature* (2025).

[46] Rafael Reisenhofer, Sebastian Bosse, Gitta Kutyniok, and Thomas Wiegand. 2018. A Haar Wavelet-Based Perceptual Similarity Index for Image Quality Assessment. *Signal Processing: Image Communication* (2018).

[47] Robin Rombach, Andreas Blattmann, Dominik Lorenz, Patrick Esser, and Björn Ommer. 2022. High-resolution image synthesis with latent diffusion models. In *CVPR*.

[48] Christian Schlarmann and Matthias Hein. 2023. On the Adversarial Robustness of Multi-Modal Foundation Models. In *ICCV Workshops*.

[49] Ramprasaath R Selvaraju, Michael Cogswell, Abhishek Das, Ramakrishna Vedantam, Devi Parikh, and Dhruv Batra. 2017. Grad-CAM: Visual Explanations from Deep Networks via Gradient-Based Localization. In *ICCV*.

[50] Ali Shafahi, Mahyar Najibi, Mohammad Amin Ghiasi, Zheng Xu, John Dicker-son, Christoph Studer, Larry S Davis, Gavin Taylor, and Tom Goldstein. 2019. Adversarial Training for Free!. In *NeurIPS*, Vol. 32.

[51] Hamid R Sheikh and Alan C Bovik. 2006. Image Information and Visual Quality. *IEEE Transactions on Image Processing* (2006).

[52] Amanpreet Singh, Vivek Natarajan, Meet Shah, Yu Jiang, Xinlei Chen, Dhruv Batra, Devi Parikh, and Marcus Rohrbach. 2019. Towards VQA Models That Can Read. In *CVPR*.

[53] Haoqin Tu, Chenhang Cui, Zijun Wang, Yiyang Zhou, Bingchen Zhao, Junlin Han, Wangchunshu Zhou, Huaxiu Yao, and Cihang Xie. 2024. How Many Unicorns Are in This Image? A Safety Evaluation Benchmark for Vision LLMs. In *ECCV*.

[54] Haodi Wang, Kai Dong, Zhilei Zhu, Haotong Qin, Aishan Liu, Xiaolin Fang, Jiakai Wang, and Xianglong Liu. 2024. Transferable Multimodal Attack on Vision-Language Pre-training Models. In *IEEE S&P*.

[55] Xunguang Wang, Zhenlan Ji, Pingchuan Ma, Zongjie Li, and Shuai Wang. 2024. InstructTA: Instruction-Tuned Targeted Attack for Large Vision-Language Models. *arXiv preprint arXiv:2312.01886* (2024).

[56] Yubo Wang, Chaohu Liu, Yanqiu Qu, Haoyu Cao, Deqiang Jiang, and Linli Xu. 2024. Break the Visual Perception: Adversarial Attacks Targeting Encoded Visual Tokens of Large Vision-Language Models. In *ACM MM*.

[57] Zhou Wang, Alan C Bovik, Hamid R Sheikh, and Eero P Simoncelli. 2004. Image Quality Assessment: From Error Visibility to Structural Similarity. *IEEE Transactions on Image Processing* (2004).

[58] Zhibo Wang, Hengchang Guo, Zhefei Zhang, Wenxin Liu, Zhan Qin, and Kui Ren. 2021. Feature Importance-aware Transferable Adversarial Attacks. In *ICCV*.

[59] Zhou Wang, Eero P Simoncelli, and Alan C Bovik. 2003. Multiscale Structural Similarity for Image Quality Assessment. In *Asilomar Conference on Signals, Systems and Computers*.

[60] Zeyu Wang, Cihang Xie, Brian Bartoldson, and Bhavya Kailkhura. 2025. Double Visual Defense: Adversarial Pre-training and Instruction Tuning for Improving Vision-Language Model Robustness. *arXiv preprint arXiv:2501.09446* (2025).

[61] Zhipeng Wei, Jingjing Chen, Micah Goldblum, Zuxuan Wu, Tom Goldstein, and Yu-Gang Jiang. 2022. Towards Transferable Adversarial Attacks on Vision Transformers. In *AAAI*.

[62] Chaoyi Wu, Weixiong Lin, Xiaoman Zhang, Ya Zhang, Weidi Xie, and Yanfeng Wang. 2024. PMC-LLaMA: Toward Building Open-Source Language Models for Medicine. *Journal of the American Medical Informatics Association* (2024).

[63] Sophie Xhonneux, Alessandro Sordoni, Stephan Günemann, Gauthier Gidel, and Leo Schwinn. 2024. Efficient Adversarial Training in LLMs with Continuous Attacks. In *NeurIPS*.

[64] Hui Xia, Rui Zhang, Zi Kang, Shuliang Jiang, and Shuo Xu. 2024. Enhance Stealthiness and Transferability of Adversarial Attacks with Class Activation Mapping Ensemble Attack. In *NDSS*.

[65] Cihang Xie, Zhishuai Zhang, Yuyin Zhou, Song Bai, Jianyu Wang, Zhou Ren, and Alan L. Yuille. 2019. Improving Transferability of Adversarial Examples with Input Diversity. In *CVPR*.

[66] Peng Xie, Yequan Bie, Jianda Mao, Yangqiu Song, Yang Wang, Hao Chen, and Kani Chen. 2025. Chain of Attack: On the Robustness of Vision-Language Models Against Transfer-Based Adversarial Attacks. In *CVPR*.

[67] Weilin Xu, David Evans, and Yanjun Qi. 2018. Feature Squeezing: Detecting Adversarial Examples in Deep Neural Networks. In *NDSS*.

[68] Dingchen Yang, Bowen Cao, Anran Zhang, Weibo Gu, Winston Hu, and Guang Chen. 2025. Beyond Intermediate States: Explaining Visual Redundancy through Language. *arXiv preprint arXiv:2503.20540* (2025).

[69] Peter Young, Alice Lai, Micah Hodosh, and Julia Hockenmaier. 2014. From Image Descriptions to Visual Denotations: New Similarity Metrics for Semantic Inference over Event Descriptions. *Transactions of the Association for Computational Linguistics* (2014).

[70] Xiaohua Zhai, Basil Mustafa, Alexander Kolesnikov, and Lucas Beyer. 2023. Sigmoid Loss for Language Image Pre-training. In *ICCV*.

[71] Jianping Zhang, Yizhan Huang, Weibin Wu, and Michael R. Lyu. 2023. Transferable Adversarial Attacks on Vision Transformers with Token Gradient Regularization. In *CVPR*.

[72] Lin Zhang, Lei Zhang, Xuanqin Mou, and David Zhang. 2011. FSIM: A Feature Similarity Index for Image Quality Assessment. *IEEE Transactions on Image Processing* (2011).

[73] Richard Zhang, Phillip Isola, Alexei A Efros, Eli Shechtman, and Oliver Wang. 2018. The Unreasonable Effectiveness of Deep Features as a Perceptual Metric. In *CVPR*.

[74] Xinwei Zhang, Hangcheng Liu, Li Bai, Hao Wang, Qingqing Ye, Tianwei Zhang, and Haibo Hu. 2026. On the Adversarial Robustness of Large Vision-Language Models under Visual Token Compression. *arXiv preprint arXiv:2601.21531* (2026).

[75] Xinlu Zhang, Yujie Lu, Weizhi Wang, An Yan, Jun Yan, Lianke Qin, Heng Wang, Xifeng Yan, William Yang Wang, and Linda Ruth Petzold. 2023. Gpt-4v (ision) as a generalist evaluator for vision-language tasks. *arXiv preprint arXiv:2311.01361* (2023).

[76] Chenyang Zhao, Kun Wang, Xingyu Zeng, Rui Zhao, and Antoni B Chan. 2024. Gradient-Based Visual Explanation for Transformer-based CLIP. In *ICML*.

[77] Yunqing Zhao, Tianyu Pang, Chao Du, Xiao Yang, Chongxuan Li, Ngai-Man Cheung, and Min Lin. 2023. On Evaluating Adversarial Robustness of Large Vision-Language Models. In *NeurIPS*.

[78] Deyao Zhu, Jun Chen, Xiaoqian Shen, Xiang Li, and Mohamed Elhoseiny. 2024. MiniGPT-4: Enhancing Vision-Language Understanding with Advanced Large Language Models. In *ICLR*.

[79] Jinguo Zhu, Weiyun Wang, Zhe Chen, Zhaoyang Liu, Shenglong Ye, Lixin Gu, Hao Tian, Yuchen Duan, Weijie Su, Jie Shao, et al. 2025. InternVL3: Exploring Advanced Training and Test-Time Recipes for Open-Source Multimodal Models. *arXiv preprint arXiv:2504.10479* (2025).

A Appendix Overview

We briefly outline the appendix structure. Section B lists the key notation, and Section C reviews related work. Section D presents additional attack scenarios and a medical-diagnosis case study. Section E provides pseudocode for SGMA, and Section F presents qualitative visual illustrations. Section G details the experimental setup, while Section H reports additional experimental results. Finally, Section I discusses possible defenses, compatibility with model ensembles, extensions to targeted attacks, and limitations.

B Notation

We provide the frequently used notation throughout this paper for reference in Table 4.

Table 4: Notation used throughout the paper.

Symbol	Description
I	Input image
T_d	Text description corresponding to the I
I_{adv}	Adversarial image ($I + \delta$)
v, t	Normalized image and text embeddings
d	Shared alignment dimension (after projection)
d_v	Vision encoder hidden dimension (before projection)
R	Input image resolution
$H \times W$	Patch grid size
A	Patch-level attention map
M	Pixel-level semantic mask
ϵ_{map}	Pixel-wise perturbation map
ϵ	Average per-pixel perturbation budget
r	Base ratio for uniform vs. focused allocation
$f_v(\cdot)$	CLIP vision encoder
$f_t(\cdot)$	CLIP text encoder
$f_v^{\text{all}}(\cdot)$	All visual tokens from vision encoder (before projection)
$f_v^{\text{patch}}(\cdot)$	Patch visual tokens from vision encoder (excluding [CLS])

C Related Work

Adversarial Attacks on LVLMs. With the growing deployment of LVLMs, their vulnerability to adversarial image examples has attracted increasing attention. Early studies primarily adopt end-to-end white-box optimization, directly backpropagating through the entire model to manipulate outputs. For example, Schlarbmann and Hein [48] minimize output-level losses to craft perturbations. While effective, these methods require full access to the model parameters and are computationally expensive, limiting their practicality.

To improve efficiency, subsequent work has shifted toward encoder-based attacks, which perturb only the vision encoder [74]. Representative approaches include minimizing the cosine similarity between adversarial features and target text embeddings [10], maximizing the distance between clean and adversarial representations [13], and disrupting patch-wise, relational, and global semantics via multi-level objectives [56]. These methods are more lightweight and generalizable, but most of them implicitly assume that the surrogate encoder used in crafting perturbations is identical or similar to the one employed in the victim LVLM. Such an assumption is increasingly unrealistic, as modern LVLMs adopt diverse and often proprietary visual backbones and fusion mechanisms.

To date, only a few studies have attempted to enhance encoder-based transferability under black-box settings. For example, Zhao et al. [77] refine perturbations using feedback from the victim model, though at the cost of high query overhead and detection risk. Xie et al. [66] employ an auxiliary captioning model to produce semantic labels as intermediate targets, which serve as auxiliary signals for crafting perturbations. However, this method still relies on partial architectural or semantic alignment, and effectively assumes that the surrogate vision encoder is similar to that of the victim LVLM. Dong et al. [13] adopt model ensembling, a widely used strategy to boost adversarial transferability across vision models, to improve cross-encoder alignment. However, despite such efforts, encoder-based transferability under the zero-query black-box setting remains largely unexplored. In this work, we conduct a systematic investigation to address this gap.

Transfer-based Attacks. Prior research on transfer-based adversarial attacks in vision tasks has proposed several strategies to enhance transferability. Most approaches are general-purpose and apply across different vision models, including *ensemble-model* attacks that optimize over multiple surrogates [34], *momentum*-based updates that stabilize and amplify gradient directions [14], and *input-transformation* strategies (e.g., random resize/crop, input diversity) that improve robustness to model variations [65]. In addition, model-specific techniques have been designed for vision transformers, such as perturbing the [CLS] token [61, 71]. While effective in image classification, these ViT-specific strategies are difficult to extend to LVLMs, which rely on distributed patch-level features for cross-modal alignment rather than a single [CLS] representation. In contrast, general-purpose transfer strategies remain broadly compatible with LVLMs, but they do not directly address the unique challenges of encoder-based transferability, which remains largely unexplored. Our work complements these lines by studying encoder-based transferability for LVLMs under zero-query constraints and targeting LVLM-specific factors.

D Attack Scenarios

The practical feasibility of adversarial attacks poses serious risks when LVLMs are deployed in safety- and security-critical domains such as medical image analysis [17, 23, 45, 62] and autonomous driving perception systems [8]. In medical applications, an adversary could introduce imperceptible perturbations at various points in the imaging pipeline, e.g., via compromised scanners, storage systems, or network infrastructure [36]. Such perturbations may cause LVLMs to produce misleading diagnostic outputs, potentially leading to erroneous clinical decisions. In autonomous driving, perturbed images could alter the model’s interpretation of traffic signs or critical objects, leading to unsafe control decisions or failures in threat detection [5]. These scenarios illustrate the real-world risks posed by transferable adversarial examples against LVLMs, which we further substantiate through a case study on medical image diagnosis.

Case Study on Medical Diagnostic. We conduct a case study on the COVID-19 Radiography dataset [2] to demonstrate the *real-world risks* of adversarial attacks in safety-critical domains. This case mimics a typical *medical diagnostic setting*, where chest X-ray images must be classified into clinically relevant categories to guide

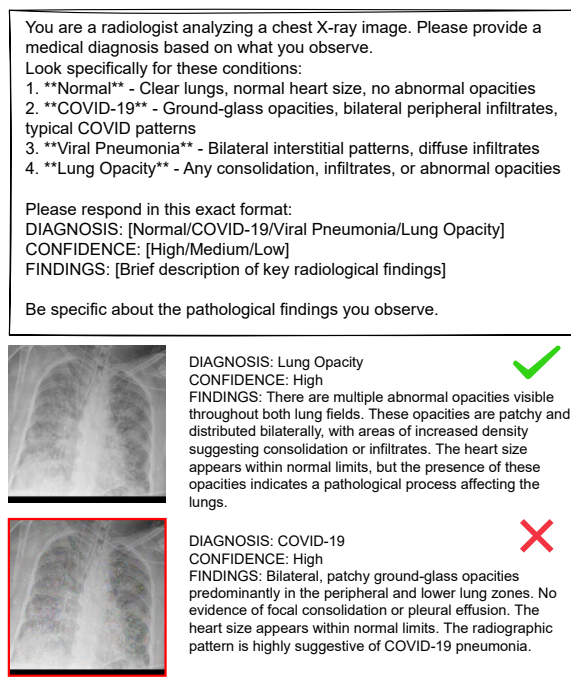


Figure 5: Illustration of diagnostic errors on chest X-ray images generated by SGMA. The top image is correctly diagnosed as Lung Opacity, while the bottom image is misclassified as COVID-19 with high confidence.

radiologists in disease identification and treatment decisions. We construct the evaluation set by sampling 100 chest X-ray images evenly across four diagnostic categories: Normal, COVID-19, Viral Pneumonia, and Lung Opacity. On this set, we apply our proposed attack, SGMA, to generate adversarial counterparts under the same configuration described in Section 6.1, and we quantify its effectiveness using the ASR, where a diagnostic misclassification is regarded as a successful attack. We evaluate the impact of these adversarial examples on GPT-4.1, treated as the victim model, with a structured radiology-style diagnostic prompt shown in Figure 5.

Results. SGMA achieves an ASR of **61%**, highlighting the alarming susceptibility of LLM-based diagnostic systems to adversarial manipulation in realistic clinical settings. Beyond the aggregate number, the adversarial perturbations lead to particularly concerning high-stakes errors. Figure 5 illustrates one such case: on the clean image, GPT-4.1 outputs “DIAGNOSIS: Lung Opacity, CONFIDENCE: High”, accompanied by findings describing multiple abnormal opacities and bilateral consolidations. Under adversarial perturbation, however, the same image is misclassified as “DIAGNOSIS: COVID-19, CONFIDENCE: High”, with fabricated findings such as “bilateral, patchy ground-glass opacities predominantly in the peripheral and lower lung zones.” From a clinical perspective, lung opacity and COVID-19 are already challenging to distinguish, and such adversarially induced misclassification, presented with

Algorithm 1 Semantic-Guided Multimodal Attack (SGMA)

Input: Clean image I , steps K , step size α , perturbation budget ϵ , base ratio r , relevance threshold τ
Output: Adversarial image I_{adv}

- 1: **# Step 1: Semantic Relevance Perturbation**
- 2: Generate description caption T_d of image I via a proxy LLM.
- 3: Compute the semantic mask \mathbb{M}
- 4: Generate the perturbation allocation map ϵ_{map} using Equation (4) with base ratio r
- 5: **# Step 2: Semantic Grounding Disruption**
- 6: Extract noun phrases $\{p_n\}_{n=1}^N$ from T_d
- 7: **for** each phrase p_n **do**
- 8: Identify aligned patch indices \mathcal{R}_n based on relevance threshold τ
- 9: Compute phrase-specific center c_n from clean patch features over \mathcal{R}_n
- 10: **end for**
- 11: Initialize perturbation $\delta \leftarrow 0$ and adversarial image $I_{\text{adv}} \leftarrow I + \delta$
- 12: **for** $t = 1$ to K **do**
- 13: Compute total loss: $\mathcal{L}_{\text{total}} = \mathcal{L}_{\text{text-image}} + \mathcal{L}_{\text{image-image}} + \mathcal{L}_{\text{local}}$
- 14: Gradient ascent: $\delta \leftarrow \delta + \alpha \cdot \text{sign}(\nabla_{\delta} \mathcal{L}_{\text{total}})$
- 15: Budget clipping: $\delta \leftarrow \text{clip}(\delta, -\epsilon_{\text{map}}, \epsilon_{\text{map}})$
- 16: Update adversarial image: $I_{\text{adv}} \leftarrow I + \delta$
- 17: **end for**
- 18: **return** I_{adv}

high confidence and detailed but spurious radiological descriptions, can be especially misleading for medical decision-making.

Implications. These results demonstrate that even imperceptible perturbations can induce systematic and confident misdiagnoses in medical scenarios. Such failures pose direct threats to clinical decision-making, as adversarially manipulated images could mislead radiologists or automated triage systems, ultimately endangering patient safety. In practice, an adversary could embed perturbations at multiple stages of the imaging pipeline, for instance by compromising X-ray scanners, tampering with picture archiving and communication systems (PACS) used in hospitals, or injecting malicious noise during cloud-based storage and transmission [36]. Once introduced, these perturbations may cause LLMs to output misleading diagnoses that could result in inappropriate treatments (e.g., unnecessary isolation, antiviral medication) or delayed care for the true underlying condition.

This case study highlights that adversarial attacks represent not only an academic concern but a tangible threat to medical AI deployments. The ability to covertly alter diagnostic outputs without raising visual suspicion underscores the urgent need for robust defenses, including adversarial training, input verification, and end-to-end security auditing, before deploying LLMs in safety- and security-critical applications.

E Pseudocode of SGMA

We present the detailed pseudocode of SGMA in Algorithm 1.

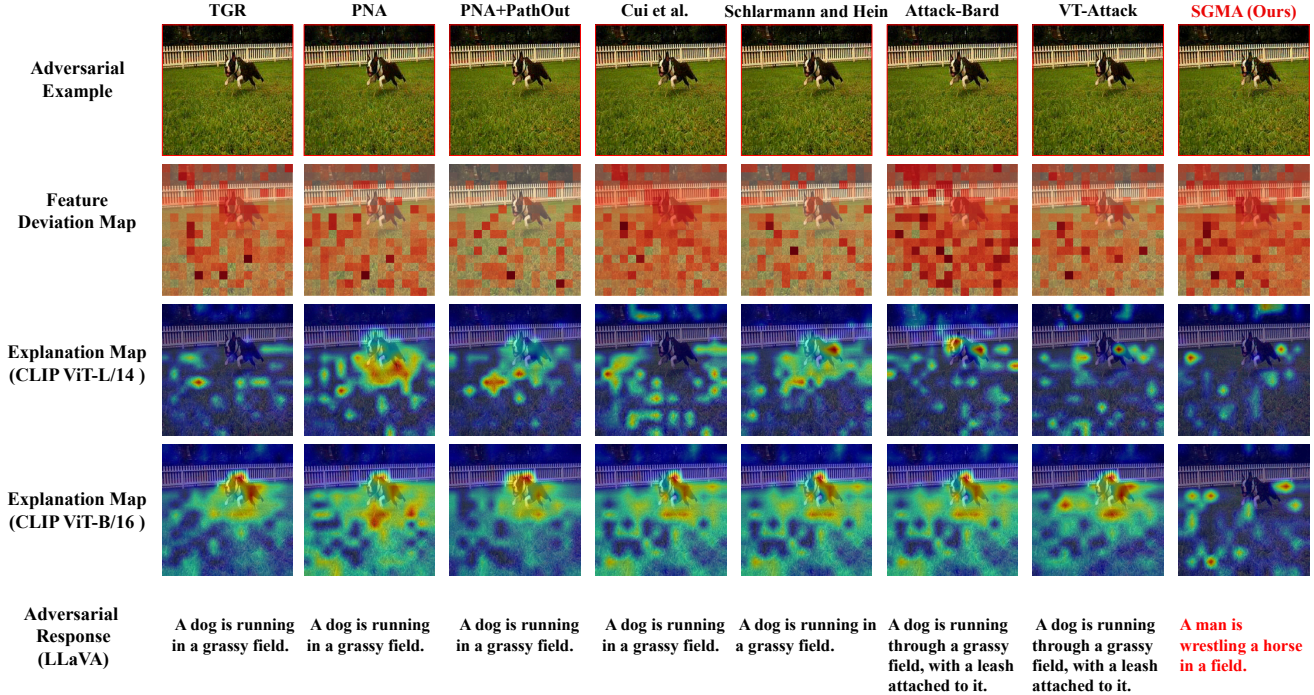


Figure 6: Qualitative comparison of adversarial effectiveness across different attack methods.

F Visual Illustration

To understand SGMA’s superior performance, we compare adversarial examples in Figures 6 and 7 with three complementary views: (1) Feature deviation maps, showing patch-wise changes in CLIP ViT-L/14 visual embeddings relative to the clean image. (2) Explanation maps computed using Grad-ECLIP[76] with the same CLIP ViT-L/14 encoders used as the surrogate during attack generation. (3) Explanation maps computed using Grad-ECLIP[76] with a different CLIP ViT-B/16 encoders, allowing us to examine whether perturbation effects persist across encoders that differ from the surrogate. The results reveal distinct perturbation patterns.

As shown in Figure 6, methods such as Schlar mann and Hein [48] and VT-Attack [56] make weak, scattered changes that leave critical foreground objects (e.g., the dog) largely intact. Others, like Cui et al. [10] and Attack-Bard [13], perturb the object more strongly but also waste budget on irrelevant background areas such as grass, limiting their impact on alignment. Notably, for these methods, the explanation maps on the surrogate encoder often show some attention shift, but this effect largely disappears when visualized with a different encoder, where attention remains centered on the main object. In contrast, SGMA focuses perturbations on semantically important regions, avoids unnecessary background changes, and produces substantial feature deviations in key areas. Even under a different encoder from the surrogate, SGMA’s explanation maps still exhibit pronounced attention shifts away from the correct object (e.g., “dog”), indicating a stronger and more persistent disruption of cross-modal grounding.

Table 5: Victim Models

Model	Link
Blip-2	Salesforce/blip2-opt-2.7b
LLaVA	llava-hf/llava-1.5-7b-hf
Qwen2.5-VL	Qwen/Qwen2.5-7B-Instruct
InternVL3	OpenGVLab/InternVL3-8B
OpenFlamingo	OpenFlamingo-4B-vitl-rpj3b-langinstruct
Kimi-VL	Kimi-VL-A3B-Instruct
GPT-4o	gpt-4o documentation
Gemini	Gemini 2.0 Flash

G Detailed Experimental Setup

Evaluation Attacks. We evaluate four representative untargeted attacks on LVLMs, including one end-to-end and three encoder-based approaches:

- Schlar mann and Hein [48] introduce an end-to-end white-box attack that generates adversarial examples by minimizing the cross-entropy loss between the original and adversarial outputs of the entire LVLM. We adapt it to a black-box setting, where adversarial examples are crafted on BLIP-2 and then transferred to other LVLMs.
- Cui et al. [10] design an encoder-based attack that generates adversarial examples by minimizing the cosine similarity between visual features of the adversarial image and the corresponding text embedding.

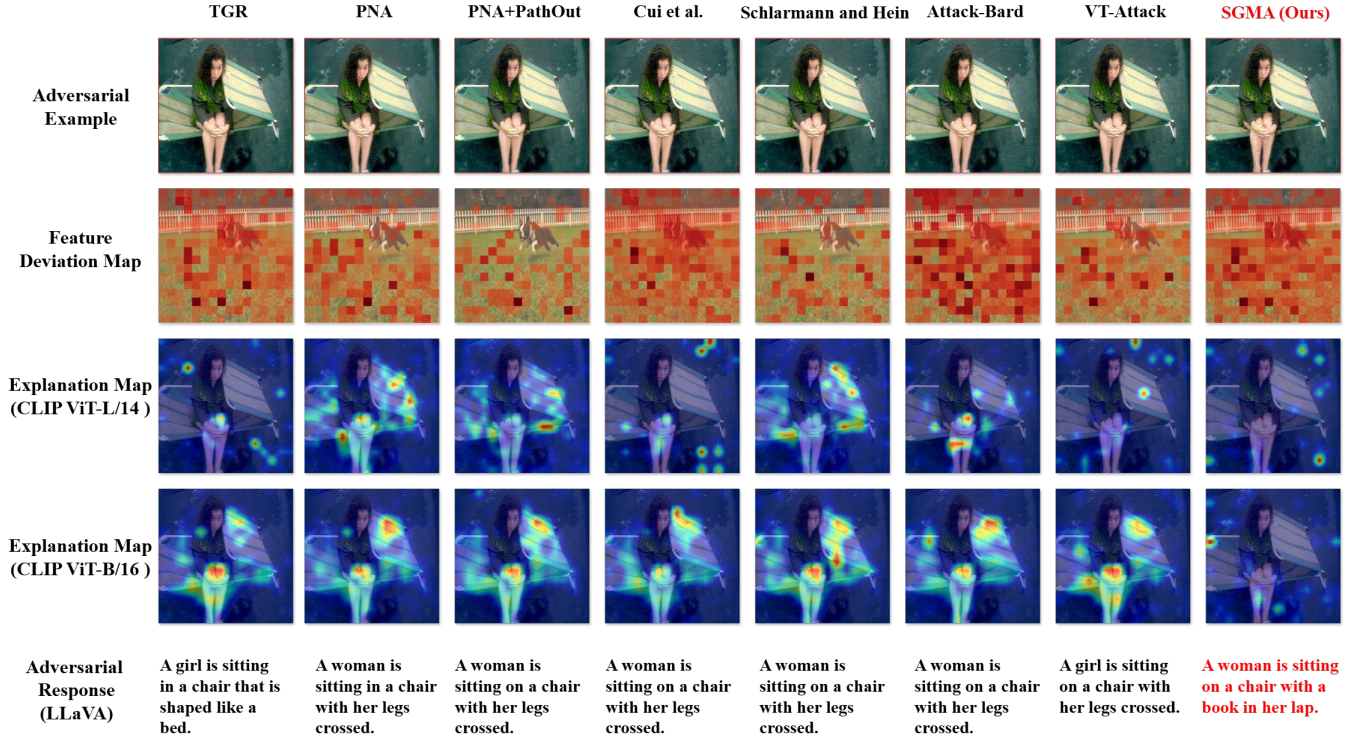


Figure 7: Qualitative comparison of adversarial effectiveness across different attack methods.

- Attack-Bard [13] is an encoder-based attack that maximizes the distance between clean and adversarial visual features, pushing the adversarial image representation away from the original visual backbone encoding.
- VT-Attack [56] is an encoder-based attack that perturbs visual tokens from multiple perspectives, including local feature representations, inter-token relationships, and global semantics. This multi-faceted disruption is designed to more comprehensively break cross-modal alignment in LVLMs.

LVLM-As-a-Judge. We use the following prompt to determine correctness.

You are given a description: #Description

Carefully observe the provided image. Your task is to answer the following question clearly and precisely:

Can the description be reasonably used to describe the content of the image, even if it does not cover all objects or details? Answer "Yes" if the description is a plausible and relevant description of the image as a whole. Otherwise, answer "No".

Answer in the following format: Match with image: <Yes/No>

When the model outputs "Match with image: No", it indicates that the adversarial description no longer aligns with the image content. We then compute the attack success rate (ASR) as the fraction of adversarial examples judged as No over the total number of evaluated cases.

Remark G.1. We adopt an LVLM-as-a-judge protocol because image captioning is an open-ended, one-to-many task: a single image admits many valid descriptions, and lexical-overlap metrics can be poorly aligned with whether a caption is *faithful* to the image. An LVLM judge can directly assess semantic and visual consistency, and prior work has shown that GPT-4V can serve as a general-purpose evaluator [75]. Our evaluation is designed to mitigate potential judge-induced biases in two ways: (1) The judge is provided with the clean image and the adversarial/clean model outputs only, and never observes the adversarial image, avoiding being confounded by the perturbation itself; (2) We use the judge LVLM that is architecturally different from the victim model to reduce same-model bias. Recent work also confirms that such LVLM-based evaluation protocols are reliable and demonstrate high alignment with human judgment [7].

Surrogate and Victim Models. For the surrogate model, we adopt the widely used CLIP ViT-L/14 for all encoder-based attacks [56, 77], while BLIP-2 serves as the surrogate model for end-to-end attacks. For victim models, we select several representative LVLMs with diverse visual encoders. Specifically, both LLaVA [32] and Open-Flamingo [4] adopt CLIP ViT-L/14 [44], while BLIP-2 [28] uses EVA-CLIP [18]. Qwen2.5-VL [43] uses a native dynamic resolution ViT tailored for high-resolution understanding. InternViT [79] is built upon InternViT, a hierarchical vision backbone optimized for multimodal fusion. Kimi-VL [25] leverages MoonViT, which supports native-resolution input and efficient scaling via a mixture-of-experts framework. Additionally, we include two popular commercial black-box LVLMs, GPT-4o [41] and Gemini 2.0

Table 6: The attack performance on more LVLMs. Bold indicates the best performance (lowest similarity or highest ASR). The end-to-end attack [48] performs particularly well on BLIP-2, as the adversarial examples are generated directly on BLIP-2 in a white-box setting.

Victim LVLM	Attack	CLIP Similarity between image and generated text ↓						ASR (%) ↑
		RN-50	RN-101	ViT-B/16	ViT-B/32	ViT-L/14	Ensemble	
InternVL3	Clean	0.2595	0.4870	0.3240	0.3155	0.2791	0.3330	-
	TGR [71]	0.2550	0.4809	0.3166	0.3100	0.2683	0.3262	22.0
	PNA [61]	0.2567	0.4825	0.3184	0.3129	0.2717	0.3284	18.8
	PNA + PathOut [61]	0.2589	0.4841	0.3213	0.3159	0.2752	0.3311	13.4
	Cui et al. [10]	0.2534	0.4803	0.3159	0.3099	0.2682	0.3255	24.6
	Schlarmann and Hein [48]	0.2552	0.4808	0.3168	0.3098	0.2695	0.3264	23.0
	Attack-Bard [13]	0.2535	0.4798	0.3146	0.3087	0.2663	0.3246	24.2
	VT-Attack [56]	0.2509	0.4776	0.3125	0.3066	0.2632	0.3222	31.6
	SGMA	0.2474	0.4735	0.3072	0.3026	0.2574	0.3176	41.2
	Clean	0.2431	0.4715	0.3096	0.3009	0.2680	0.3186	-
OpenFlamingo	TGR [71]	0.1615	0.3878	0.2116	0.2100	0.1501	0.2242	95.0
	PNA [61]	0.2118	0.4367	0.2672	0.2654	0.2145	0.2791	53.4
	PNA + PathOut [61]	0.2318	0.4577	0.2911	0.2880	0.2430	0.3023	70.9
	Cui et al. [10]	0.1598	0.3850	0.2108	0.2098	0.1501	0.2231	97.0
	Schlarmann and Hein [48]	0.2272	0.4544	0.2887	0.2835	0.2411	0.2990	59.4
	Attack-Bard [13]	0.1469	0.3736	0.1941	0.1959	0.1274	0.2076	97.8
	VT-Attack [56]	0.1297	0.3568	0.1785	0.1799	0.1165	0.1923	99.8
	SGMA	0.1263	0.3559	0.1765	0.1778	0.1129	0.1899	99.8
	Clean	0.2402	0.4689	0.3038	0.2984	0.2585	0.3140	-
	TGR [71]	0.2354	0.4623	0.2961	0.2933	0.2499	0.3074	23.4
BLIP-2	PNA [61]	0.2365	0.4648	0.2980	0.2943	0.2543	0.3096	21.9
	PNA + PathOut [61]	0.2372	0.4650	0.2989	0.2952	0.2545	0.3102	17.6
	Cui et al. [10]	0.2335	0.4606	0.2957	0.2913	0.2478	0.3058	26.8
	Schlarmann and Hein [48]	0.1795	0.4087	0.2339	0.2338	0.1758	0.2463	84.4
	Attack-Bard [13]	0.2330	0.4606	0.2941	0.2900	0.2455	0.3047	26.0
	VT-Attack [56]	0.2286	0.4567	0.2907	0.2862	0.2409	0.3006	27.6
	SGMA	0.2256	0.4536	0.2857	0.2833	0.2356	0.2968	38.6
	Clean	0.2438	0.4654	0.3064	0.3012	0.2612	0.3156	-
	TGR [71]	0.2411	0.4624	0.3004	0.2978	0.2555	0.3115	19.2
	PNA [61]	0.2403	0.4613	0.3005	0.2981	0.2542	0.3109	17.4
Kimi-VL	PNA + PathOut [61]	0.2409	0.4629	0.3020	0.2994	0.2560	0.3123	20.6
	Cui et al. [10]	0.2383	0.4592	0.3001	0.2956	0.2518	0.3090	21.8
	Schlarmann and Hein [48]	0.2382	0.4595	0.3002	0.2958	0.2512	0.3090	23.2
	Attack-Bard [13]	0.2378	0.4588	0.2993	0.2950	0.2510	0.3084	23.0
	VT-Attack [56]	0.2383	0.4586	0.2986	0.2947	0.2505	0.3082	28.2
	SGMA	0.2347	0.4546	0.2943	0.2914	0.2438	0.3037	33.2

Flash [20], to evaluate the real-world applicability in closed-source scenarios. By including models with both similar (e.g., ViT-L/14 variants) and distinct (e.g., MoonViT, interViT) visual encoders and different LLMs, we aim to comprehensively assess transferability. Table 5 gives the victim models and the corresponding link for the reproduction of the results. The details of the victim models can be found in each link.

Prompt Details. For image classification on CIFAR-10, we use the following instruction prompt:

You are an image classifier.
Given an image, classify it into exactly one of these 10 categories:
airplane | automobile | bird | cat | deer | dog | frog | horse | ship | truck.

Respond with only the category name.

For OpenFlamingo, we instead adopt the shorter template “a photo of a”, as its instruction-following capability is relatively limited.

Table 7: ASR (%) on image classification task and VQA task.

Attack	LLaVA	Qwen2.5-VL	InternVL3	OpenFlamingo	BLIP-2	Kimi-VL	GPT-4o	Gemini 2.0	Average
<i>Task: Image Classification</i>									
Clean	7.2	9.6	17.2	54.0	28.4	13.4	2.2	8.0	17.5
TGR [71]	49.2	42.4	58.4	98.2	69.8	45.0	27.4	24.6	51.9
PNA [61]	18.8	25.0	35.8	91.8	40.2	23.8	9.6	16.6	32.7
PNA + PathOut [61]	17.6	23.4	30.6	78.6	38.2	22.8	11.4	16.0	29.4
Cui et al. [10]	47.4	38.2	55.2	98.4	68.0	42.2	26.2	23.2	50.0
Schlarmann and Hein [48]	21.2	28.4	45.4	71.6	82.8	28.0	12.4	15.4	38.2
Attack-Bard [13]	29.6	38.8	51.8	79.4	55.0	50.8	21.0	22.6	43.4
VT-Attack [56]	64.2	47.0	61.8	100.0	82.8	53.0	27.2	27.4	57.4
SGMA	65.2	51.0	67.4	99.6	84.0	54.6	32.0	31.8	60.7
<i>Task: VQA</i>									
Clean	51.2	19.4	41.6	90.0	88.8	8.0	19.4	17.2	41.4
TGR [71]	59.2	53.6	56.0	97.6	91.2	53.4	37.8	37.0	60.7
PNA [61]	61.0	56.4	53.5	95.6	91.8	52.4	38.0	34.6	60.4
PNA + PathOut [61]	59.6	54.2	52.4	94.2	90.2	51.8	38.4	35.8	59.5
Cui et al. [10]	60.6	53.2	54.6	97.8	90.8	54.8	37.6	36.8	60.7
Schlarmann and Hein [48]	58.8	52.8	54.2	93.0	90.8	51.0	38.0	34.8	62.6
Attack-Bard [13]	63.2	55.0	56.0	97.4	92.4	55.8	41.4	38.0	62.4
VT-Attack [56]	61.6	55.6	56.6	98.2	91.0	54.2	39.8	37.6	61.7
SGMA	64.2	58.4	60.2	98.2	93.6	56.2	43.0	38.0	64.5

Table 8: Comparison of attack imperceptibility.

Attack	SSIM \uparrow	LPIPS \downarrow	MS-SSIM \uparrow	FSIM \uparrow	VIF \uparrow	HaarPSI \uparrow
Clean	1	0	1	1	1	1
TGR [71]	0.8943	0.0428	0.9828	0.7967	0.6383	0.9387
PNA [61]	0.8596	0.0619	0.9743	0.7835	0.5933	0.9132
PNA + PathOut [61]	0.9086	0.0379	0.9832	0.8320	0.6852	0.9401
Cui et al. [10]	0.8978	0.0406	0.9835	0.7991	0.6444	0.9395
Schlarmann and Hein [48]	0.9063	0.0378	0.9856	0.8079	0.6604	0.9450
Attack-Bard [13]	0.8924	0.0397	0.9833	0.7976	0.6433	0.9393
VT-Attack [56]	0.8978	0.0411	0.9836	0.7988	0.6440	0.9392
SGMA	0.9161	0.0369	0.9857	0.8095	0.6775	0.9336

H Additional Experimental Results

H.1 Additional Attack Performance

To provide a more comprehensive evaluation, we include additional results on diverse LVLMs and tasks beyond the main paper.

Attack Performance on More LVLMs. Table 6 reports the attack performance on several open-source LVLMs not covered in the main tables. These include models with more diverse architectures, parameter scales. The results further verify that SGMA maintains strong transferability and semantic disruption capabilities across a broad range of black-box settings.

Attack Performance on Other Tasks. Table 7 presents the performance of the proposed attack under different multimodal tasks, including visual question answering (VQA) and captioning. We observe that while captioning tasks often rely on patch-level information, VQA performance is more sensitive to subtle region–text alignments, which are effectively disrupted by our method. These

results confirm that SGMA is versatile and effective across various task types.

H.2 Attack Imperceptibility

To assess human imperceptibility, we adopt widely used full-reference image quality metrics. Higher values of SSIM [57], MS-SSIM [59], FSIM [72], VIF [51], and HaarPSI [46] indicate better preservation of structural, feature, and visual fidelity relative to the clean image, while lower LPIPS [73] values indicate smaller perceptual differences in deep feature space. As shown in Table 8, SGMA achieves the best performance across most perceptual metrics. The results demonstrate that, despite significantly improving attack effectiveness, our method does not compromise stealthiness. SGMA explicitly constrains perturbations to semantically important regions, guided by both spatial and frequency cues. While this introduces slightly more localized changes compared to uniformly distributed or less

Table 9: Effect of different surrogate models. Bold denotes best performance.

Surrogate	Attack	CLIP Similarity between image and generated text ↓						ASR (%) ↑
		RN-50	RN-101	ViT-B/16	ViT-B/32	ViT-L/14	Ensemble	
CLIP-L/14	Cui et al. [10]	0.2365	0.4584	0.2981	0.2925	0.2530	0.3077	41.8
	Attack-Bard [13]	0.2354	0.4568	0.2964	0.2915	0.2498	0.3060	38.4
	VT-Attack [56]	0.2330	0.4544	0.2939	0.2892	0.2462	0.3033	46.0
	SGMA	0.2282	0.4493	0.2873	0.2831	0.2376	0.2971	55.4
CLIP-B/16	Cui et al. [10]	0.2410	0.4624	0.3042	0.2991	0.2592	0.3132	28.4
	Attack-Bard [13]	0.2424	0.4644	0.3040	0.2998	0.2610	0.3143	21.0
	VT-Attack [56]	0.2410	0.4624	0.3042	0.2991	0.2592	0.3132	28.4
	SGMA	0.2396	0.4599	0.2999	0.2964	0.2560	0.3104	36.6
SigLIP	Cui et al. [10]	0.2416	0.4642	0.3058	0.3003	0.2616	0.3147	19.8
	Attack-Bard [13]	0.2409	0.4625	0.3039	0.2991	0.2606	0.3134	24.6
	VT-Attack [56]	0.2407	0.4614	0.3029	0.2978	0.2579	0.3121	28.4
	SGMA	0.2388	0.4614	0.3028	0.2969	0.2581	0.3116	34.2

Table 10: Effect of base ratio r .

r	Victim LVLM	CLIP Similarity Score between image and generated text (↓)						ASR (%) (↑)
		RN-50	RN-101	ViT-B/16	ViT-B/32	ViT-L/14	Ensemble	
0.2	LLaVA	0.2279	0.4481	0.2861	0.2822	0.2347	0.2958	56.0
	Qwen2.5-VL	0.2468	0.4724	0.3064	0.3010	0.2524	0.3158	37.8
	InternVL3	0.2460	0.4720	0.3038	0.3010	0.2551	0.3156	41.4
0.4	LLaVA	0.2302	0.4495	0.2880	0.2846	0.2369	0.2978	55.4
	Qwen2.5-VL	0.2468	0.4732	0.3052	0.3014	0.2516	0.3156	39.0
	InternVL3	0.2462	0.4718	0.3052	0.3013	0.2559	0.3161	41.2
0.6	LLaVA	0.2302	0.4511	0.2891	0.2848	0.2383	0.2987	51.2
	Qwen2.5-VL	0.2483	0.4743	0.3077	0.3037	0.2551	0.3178	36.4
	InternVL3	0.2498	0.4741	0.3075	0.3046	0.2586	0.3190	38.6
0.8	LLaVA	0.2305	0.4516	0.2893	0.2861	0.2404	0.2996	50.4
	Qwen2.5-VL	0.2490	0.4758	0.3093	0.3046	0.2562	0.3190	34.6
	InternVL3	0.2499	0.4751	0.3083	0.3030	0.2592	0.3191	39.0
1.0	LLaVA	0.2313	0.4527	0.2923	0.2872	0.2442	0.3015	48.8
	Qwen2.5-VL	0.2512	0.4772	0.3117	0.3062	0.2586	0.3209	31.2
	InternVL3	0.2511	0.4770	0.3102	0.3059	0.2621	0.3213	35.4

targeted perturbations, it maintains comparable perceptual quality from a human perspective.

H.3 Additional Ablation Studies and Analysis

Effect of Surrogate Models. We investigate how the architectural alignment between surrogate and victim models influences attack effectiveness. Table 9 compares the attack performance on LLaVA using different attacks and surrogates. Since LLaVA adopts a CLIP-L/14 backbone, employing architecturally dissimilar surrogates (e.g., SigLIP) results in a clear performance degradation. Across all different surrogates, our SGMA remains consistently superior to all baselines across metrics.

Effect of Perturbation Budget ϵ . We evaluate the performance of SGMA under varying perturbation budgets $\epsilon \in \{2, 4, 8, 12, 16\}$. As

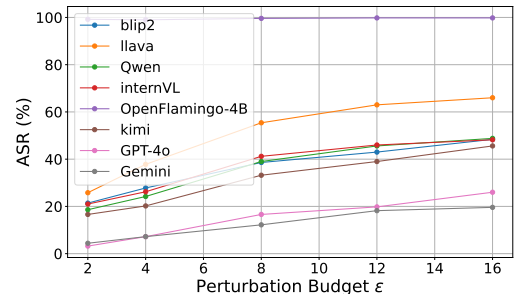
**Figure 8: Attack performance across perturbation budgets.**

Table 11: Effect of relevance threshold τ .

τ	Victim LVLM	CLIP Similarity Score between image and generated text (↓)						ASR (%) (↑)
		RN-50	RN-101	ViT-B/16	ViT-B/32	ViT-L/14	Ensemble	
0.1	LLaVA	0.2304	0.4513	0.2903	0.2859	0.2405	0.2997	52.2
	Qwen2.5-VL	0.2483	0.4742	0.3075	0.3027	0.2528	0.3171	35.4
	InternVL3	0.2467	0.4731	0.3064	0.3022	0.2549	0.3166	42.8
0.2	LLaVA	0.2293	0.4506	0.2891	0.2850	0.2381	0.2984	54.2
	Qwen2.5-VL	0.2471	0.4737	0.3064	0.3021	0.2541	0.3167	37.0
	InternVL3	0.2475	0.4736	0.3063	0.3020	0.2563	0.3171	38.8
0.3	LLaVA	0.2302	0.4495	0.2880	0.2846	0.2369	0.2978	55.4
	Qwen2.5-VL	0.2468	0.4732	0.3052	0.3014	0.2516	0.3156	39.0
	InternVL3	0.2462	0.4718	0.3052	0.3013	0.2559	0.3161	41.2
0.4	LLaVA	0.2292	0.4502	0.2874	0.2844	0.2370	0.2977	53.8
	Qwen2.5-VL	0.2469	0.4737	0.3059	0.3012	0.2524	0.3160	37.2
	InternVL3	0.2474	0.4721	0.3057	0.3009	0.2552	0.3163	40.8

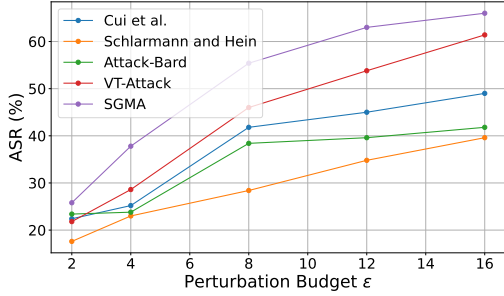


Figure 9: ASR (%) on LLaVA under varying ℓ_∞ perturbation budgets $\epsilon \in \{2, 4, 8, 12, 16\}$. Our method (SGMA) consistently outperforms existing encoder-based attacks, with sharper gains at larger ϵ .

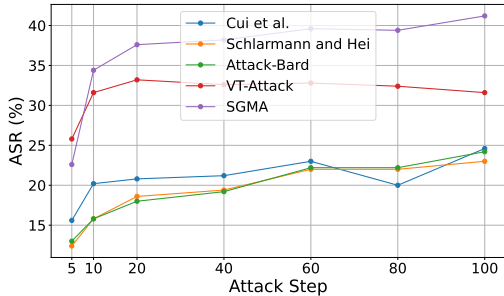


Figure 10: ASR (%) on InternVL under varying attack steps. Increasing the number of steps improves ASR for all methods, but SGMA exhibits more consistent gains and reaches the highest ASR at 100 steps.

illustrated in Figure 8, the ASR consistently increases with the perturbation magnitude across all tested LVLMs. Notably, even under

Table 12: Comparison of runtime efficiency. We report the average runtime (seconds per sample) required to generate an adversarial example.

Attack Method	Time (s/sample)
Schlarmann and Hein [48]	28.4024
Cui et al. [10]	5.5649
Attack-Bard [13]	5.8810
VT-Attack [56]	9.7486
SGMA	10.3353

a low budget (e.g., $\epsilon = 4$), SGMA achieves non-trivial ASR, demonstrating its effectiveness under tight constraints. When $\epsilon = 16$, the ASRs on GPT-4o and Gemini reach up to 20%, indicating that the attack remains effective even on more robust models. These results underscore the scalability and generalization ability of SGMA under different perturbation levels. We additionally compare the attack performance under different perturbation budgets on LLaVA in Figure 9. Across all methods, ASR increases monotonically with ϵ , indicating better attack effectiveness under larger perturbations. Notably, SGMA consistently achieves the highest ASR across all budgets. While most baselines (e.g., Cui et al., Attack-Bard) plateau around 40–50% when $\epsilon = 16$, SGMA reaches 66%, showing its stronger optimization and better alignment with downstream model behavior. These results further demonstrate SGMA’s superior performance.

Computational Cost. We evaluate the computational cost of SGMA by measuring the average runtime per sample under identical hardware and software environments. As shown in Table 12, SGMA demonstrates a significant efficiency advantage over the end-to-end baseline, achieving a 2.7 \times speedup compared to Schlarmann & Hein [48] (10.34s vs. 28.40s). This efficiency stems from our strategy of targeting the vision encoder rather than optimizing the entire VLM pipeline. Compared to other transfer-based attacks (e.g., Cui et al. [10] and Attack-Bard [13]), SGMA incurs a marginal increase in computational overhead. This is primarily due to the calculation of

the semantic relevance location. Crucially, this additional computation is a one-time cost per image, independent of the number of optimization steps, ensuring scalability. While SGMA is comparable to VT-Attack [56] in runtime, it offers superior transferability.

Generalization to Other Tasks. In order to evaluate SGMA more comprehensively, we introduce two additional tasks: image classification and VQA. As shown in Table 7 in Appendix H.1, our attack achieves consistently higher ASR across all LVLMs compared to prior methods. For image classification, SGMA attains the highest average ASR of 60.7%, surpassing all baselines. On the VQA task, SGMA achieves the top average ASR of 61.7%, demonstrating strong robustness across diverse reasoning paradigms. Besides, our perturbations are task-agnostic, generated from the full descriptive caption T_d rather than tailored to specific tasks. While task-specific perturbations that focus on task-relevant regions could further increase ASR, our task-agnostic design demonstrates consistent improvements across different tasks, indicating that SGMA effectively disrupts fundamental vision-language grounding.

Effect of Base Ratio r . We analyze the impact of the base perturbation ratio r in the pixel-wise perturbation allocation mechanism (Equation (4)). As shown in Table 10, a smaller r allocates more perturbation budget to semantically important regions, resulting in lower CLIP scores and higher ASRs. For example, when r decreases from 1.0 to 0.2, the ASR on Qwen2.5-VL improves from 31.2% to 37.8%, while the ensemble CLIP score drops from 0.3209 to 0.3158. However, excessively small r may lead to underutilization of the global image space, limiting robustness. In our experiments, we observe that $r = 0.2$ offers the best trade-off between focused perturbation and overall coverage, and we adopt it as the default setting for SGMA.

Effect of Relevance Threshold τ . We evaluate four values of the relevance threshold $\tau \in \{0.1, 0.2, 0.3, 0.4\}$ to understand its effect on attack performance. A smaller τ includes more regions, potentially introducing irrelevant areas and diluting perturbation effectiveness. In contrast, a larger τ selects fewer patches, which may hinder transferability due to overly concentrated perturbations. As shown in Table 11, $\tau = 0.3$ consistently achieves the best performance, and is thus adopted as our default setting.

Effect of Attack Steps. Adhering to the evaluation principles established in [6], we analyze the evolution of ASR over varying PGD steps to assess convergence. As illustrated in Figure 10, ASR improves with the step count for all methods before gradually saturating, indicating stable convergence under a fixed perturbation budget. While baseline methods (e.g., [10, 48]) plateau relatively early, showing negligible gains beyond 40 steps, SGMA consistently achieves superior ASR across all intervals. It maintains moderate improvements as optimization proceeds, a trajectory that suggests more effective gradient guidance rather than delayed convergence. To ensure fair comparison and eliminate optimization-related confounds, we standardize on 100 PGD steps for all main experiments, ensuring all methods are evaluated well within their stable performance regimes.

I Discussion

I.1 Possible Defenses

The potential social and security risks of our proposed attacks motivate the exploration of effective defense strategies. Following prior work [54], we focus on input-level preprocessing methods that require no access to model internals or downstream labels. Specifically, we evaluate four representative techniques: Bit-Red [67], JPEG compression [21], neural representation purification (NRP) [37], and diffusion-based purification (DiffPure) [39]. As shown in Table 13, the diffusion-based DiffPure proves to be the most effective, significantly reducing the average ASR from 43.25% (no defense) to 25.83%. JPEG compression follows as the second most effective method, lowering the average ASR to 29.39%, though its lossy nature may impact clean image quality. NRP achieves moderate improvement with an average ASR of 30.80%, whereas Bit-Red offers only marginal gains (41.95%), likely due to its limited ability to remove semantically aligned perturbations. Notably, even with strong defenses like DiffPure, attacks remain partially successful (e.g., 54.0% ASR on OpenFlamingo), underscoring the challenge of completely mitigating such threats.

Beyond preprocessing, adversarial training is another promising direction [50, 60, 63]. Recent studies have attempted to enhance robustness by adversarially training the vision encoder [19, 60], but such approaches still require large-scale data and significant computational resources, and their gains often fail to transfer fully to LVLMs. Although we do not adopt adversarial training due to resource constraints, we believe it holds promise and encourage future work on more efficient strategies for LVLMs.

I.2 Compatible with Model Ensemble

In addition to the single-surrogate setting used in our main evaluations, we extend SGMA to a model ensemble setting by integrating multiple CLIP-based surrogates throughout the attack pipeline. We use M CLIP variants, each with a visual encoder $\mathcal{I}^{(m)}(\cdot)$ and a text encoder $\mathcal{T}^{(m)}(\cdot)$, $m = 1, \dots, M$. Both the semantic relevance mask construction and the loss computation aggregate outputs from all surrogates.

Ensemble-based Mask Construction. For each model, we independently compute patch-wise semantic relevance maps and average them to obtain a more robust spatial mask:

$$\mathbb{M} = \frac{1}{M} \sum_{m=1}^M \mathbb{M}^{(m)}, \quad (11)$$

where $\mathbb{M}^{(m)}$ is the spatial semantic map from the m -th surrogate. The final mask is then used to derive the pixel-wise perturbation budget ϵ_{map} .

Ensemble-based Optimization. The total attack loss is averaged over all surrogates:

$$\mathcal{L}_{\text{total}}^{\text{ensemble}} = \frac{1}{M} \sum_{m=1}^M \left(\mathcal{L}_{\text{text-image}}^{(m)} + \mathcal{L}_{\text{image-image}}^{(m)} + \mathcal{L}_{\text{local}}^{(m)} \right), \quad (12)$$

where each term is computed using features from the corresponding surrogate. This ensemble design ensures strong transferability across diverse architectures. Moreover, SGMA is orthogonal to

Table 13: ASR (%) under different defenses.

Defense	LLaVA	Qwen2.5-VL	InternVL3	OpenFlamingo	BLIP-2	Kimi-VL	GPT-4o	Gemini 2.0	Average
No Defense	55.4	39.0	41.2	99.6	38.6	33.2	16.6	12.4	43.25
Bit-Red [67]	51.2	37.4	38.6	99.6	36.4	28.6	17.0	13.3	41.95
JPEG [21]	34.2	26.0	28.3	74.4	27.4	23.8	8.4	8.8	29.39
NRP [37]	35.8	30.4	27.0	78.6	26.6	26.8	10.0	11.2	30.80
DiffPure [39]	31.0	26.8	23.2	54.0	25.0	23.6	12.6	10.4	25.83

Table 14: Attack performance under the model-ensemble (ME) setting.

Attack	CLIP Similarity between image and generated text ↓						ASR (%) ↑
	RN-50	RN-101	ViT-B/16	ViT-B/32	ViT-L/14	Ensemble	
Cui et al. [10]	0.2341	0.4556	0.2956	0.2912	0.2487	0.3050	43.0
Attack-Bard [13]	0.2355	0.4565	0.2959	0.2916	0.2487	0.3057	34.2
VT-Attack [56]	0.2285	0.4488	0.2870	0.2830	0.2367	0.2968	52.2
SGMA	0.2228	0.4429	0.2795	0.2762	0.2265	0.2896	64.0

Table 15: ASR (%) of different targeted adversarial methods against various LVLMs.

Attack	LLaVA	Qwen2.5-VL	InternVL3	OpenFlamingo	BLIP-2	Kimi-VL	GPT-4o	Gemini 2.0	Average
MF-ii [77]	1.6	0.8	1.2	39.6	2.2	1.4	0.8	0.4	6.0
MF-it [77]	3.2	1.2	2.0	51.2	1.0	1.2	0.6	0.6	7.6
CoA [66]	4.2	1.8	2.2	34.2	2.8	1.2	0.8	0.8	6.0
SGMA	16.8	3.6	11.8	91.0	8.2	6.2	8.6	5.2	18.9

general transferability-enhancing techniques such as input diversity [65], translation invariance [15], which can be readily integrated into our optimization to further boost black-box performance.

Result. We report the attack performance in Table 14. Overall, ME consistently improves the ASR of all attacks, confirming its effectiveness as a general technique for enhancing black-box transferability. Notably, the relative advantage of SGMA further widens under ME: it achieves an additional $\sim 12\%$ ASR improvement over the best baseline, compared to $\sim 9\%$ in the single-surrogate setting.

I.3 Extension to Targeted Attacks

The analysis so far has focused on the untargeted setting, since it provides a cleaner framework to study transferability without the added complexity of specifying consistent target outputs in LVLMs. SGMA can also be extended to the targeted setting, where the goal is to let the LVLM produce a specific adversarial output T_{tgt} . We adapt the semantic relevance mask by replacing the original caption with T_{tgt} , and introduce a contrastive objective that jointly (i) repels the adversarial image from the original semantics and (ii) attracts it toward the target semantics. The targeted variant introduces two modifications.

Semantic Mask. Given the target text T_{tgt} , we modify the semantic relevance mask by replacing the original caption T_d with T_{tgt} in Section 5.2. This yields a target-aware attention map that highlights image regions semantically aligned with the target concept, allowing perturbations to be concentrated on regions relevant to the intended manipulation.

Semantic Grounding Disruption. We design a contrastive loss that simultaneously (i) pushes the adversarial image away from the original semantics and (ii) pulls it toward the target semantics. To obtain target-aligned visual features, we generate a synthetic target image I_{tgt} from T_{tgt} using a high-quality text-to-image model (e.g., Stable Diffusion [47]).

Given the clean image I , original caption T_d , target caption T_{tgt} , and target image I_{tgt} , the targeted objective consists of three terms: The text-image loss is formulated to repel the adversarial image from the original caption while attracting it to the target caption:

$$\mathcal{L}_{\text{text-image}}^{\text{targeted}} = \mathcal{L}_{\text{text-image}}(I_{\text{adv}}, T_d) - \mathcal{L}_{\text{text-image}}(I_{\text{adv}}, T_{\text{tgt}}). \quad (13)$$

Similarly, the image-image loss encourages the adversarial image to align with the target image while deviating from the original image:

$$\mathcal{L}_{\text{image-image}}^{\text{targeted}} = \mathcal{L}_{\text{image-image}}(I_{\text{adv}}, I) - \mathcal{L}_{\text{image-image}}(I_{\text{adv}}, I_{\text{tgt}}). \quad (14)$$

The local semantic loss further reinforces this objective at the patch level by contrasting the relevance of adversarial patches with respect to both original and target semantic regions:

$$\mathcal{L}_{\text{local}}^{\text{targeted}} = \mathcal{L}_{\text{local}}(I_{\text{adv}}, \mathcal{R}_n^{\text{orig}}, \mathbf{c}_n^{\text{orig}}) - \mathcal{L}_{\text{local}}(I_{\text{adv}}, \mathcal{R}_n^{\text{tgt}}, \mathbf{c}_n^{\text{tgt}}), \quad (15)$$

where $\mathcal{R}_n^{\text{orig}}$ and $\mathcal{R}_n^{\text{tgt}}$ denote the sets of semantically relevant patches derived from the original text T_d and image I , and the target text T_{tgt} and image I_{tgt} , respectively. These regions are computed following the method in Equation (7), and $\mathbf{c}_n^{\text{orig}}$ and $\mathbf{c}_n^{\text{tgt}}$ represent their corresponding feature centers.

Algorithm 2 Targeted Semantic-Guided Multimodal Attack (Targeted SGMA)

Input: Clean image I , target text T_{tgt} , steps K , step size α , perturbation budget ϵ , fusion weight λ , base ratio r , relevance threshold τ

Output: Adversarial image I_{adv}

- 1: **# Step 1: Target-aware Semantic Relevance Perturbation**
- 2: Generate I_{tgt} from T_{tgt} via a text-to-image model
- 3: Obtain T_d by describing I_{tgt} using a proxy LVLM
- 4: Compute target-aware semantic mask \mathbb{M}_{tgt} using T_{tgt} and I
- 5: Generate perturbation allocation map ϵ_{map} using Equation (4) with base ratio r
- 6: **# Step 2: Target-aware Semantic Grounding**
- 7: Extract noun phrases $\{p_n\}_{n=1}^N$ from both T_d (original) and T_{tgt} (target)
- 8: **for** each phrase p_n **do**
- 9: Identify aligned patch indices $\mathcal{R}_n^{\text{orig}}, \mathcal{R}_n^{\text{tgt}}$ from T_d and T_{tgt} , respectively
- 10: Compute corresponding feature centers $\mathbf{c}_n^{\text{orig}}, \mathbf{c}_n^{\text{tgt}}$
- 11: **end for**
- 12: Initialize perturbation $\delta \leftarrow 0$ and adversarial image $I_{adv} \leftarrow I + \delta$
- 13: **for** $t = 1$ to K **do**
- 14: Compute total contrastive loss: $\mathcal{L}_{\text{total}} = \mathcal{L}_{\text{text-image}}^{\text{targeted}} + \mathcal{L}_{\text{image-image}}^{\text{targeted}} + \mathcal{L}_{\text{local}}^{\text{targeted}}$
- 15: Gradient ascent: $\delta \leftarrow \delta + \alpha \cdot \text{sign}(\nabla_{\delta} \mathcal{L}_{\text{total}})$
- 16: Budget clipping: $\delta \leftarrow \text{clip}(\delta, -\epsilon_{map}, \epsilon_{map})$
- 17: Update adversarial image: $I_{adv} \leftarrow I + \delta$
- 18: **end for**
- 19: **return** I_{adv}

The overall targeted objective is the sum of the three terms and is optimized with respect to I_{adv} under the same per-pixel perturbation constraint as in the untargeted setting (Equation (10)). The full procedure is summarized in Algorithm 2.

Evaluation. Targeted attacks are inherently more difficult than untargeted ones, as they require driving the model toward a specific output rather than merely inducing misalignment. To evaluate our targeted SGMA, we design a simple but challenging task: misclassifying cat images as dogs. Specifically, we select 1,000 cat images from the Cat and Dog Dataset [1] and deem an attack successful only if the generated response explicitly contains the word “dog”. This success criterion requires changing the model’s decision on the *primary object*. Compared to LVLM-as-a-judge protocols that allow for partial matches [66], it yields a stricter (and lower) ASR.

We compare SGMA with representative baselines: MF-ii and MF-it [77], which improve transferability by aligning adversarial features with target image or text embeddings, and CoA [66], a recent approach that enhances transferability via iterative semantic updates guided by an auxiliary captioning model. As reported in Table 15, SGMA achieves an ASR of **18.9%** on average, exceeding the strongest baseline by more than 11%. Notably, the ASR remains limited under this strict primary-object criterion, underscoring that targeted attacks are substantially more challenging than untargeted ones. This is because targeted attacks must override the model’s

strong visual-language priors to steer generation toward a specific output, rather than merely disrupting the original alignment.

I.4 Limitations and Future Works

Although our proposed method demonstrates strong transferability in the vision-language setting, several limitations remain and open avenues for future research. ① Our current attack focuses on LVLMs and has not yet been extended to broader multimodal systems, such as audio-language models or embodied agents. Generalizing our framework to support additional modalities remains an important future direction. ② Improving the transferability of encoder-based attacks under commercial APIs remains an open challenge. This is largely due to the potential use of input filtering, non-differentiable transformations, or reinforced safety alignment (e.g., RLHF) in commercial systems, which hinder effective perturbation transfer. Future work may consider designing defense-aware attacks that explicitly account for such constraints to enhance real-world applicability. ③ Generating effective targeted adversarial examples in a zero-query black-box setting remains highly challenging due to entangled cross-modal alignments and the absence of direct gradient signals. Importantly, our method is orthogonal to common transferability enhancement techniques, such as input diversity [65] and the model ensemble, which we already utilize to improve performance. In future work, we can seamlessly integrate them into our framework to further improve the targeted transferability. ④ Our evaluation of defenses has been limited to input-level preprocessing methods, which show only marginal effectiveness. These findings underscore the need for exploring stronger defense strategies, such as adversarial training or detection mechanisms, to better safeguard LVLMs against transferable adversarial examples.